

1 **Light-absorbing black carbon and brown carbon components of smoke aerosol from**  
2 **DSCOVR EPIC measurements over North America and Central Africa**

3  
4 Myungje Choi<sup>1,2</sup>, Alexei Lyapustin<sup>2</sup>, Gregory L. Schuster<sup>3</sup>, Sujung Go<sup>1,2</sup>, Yujie Wang<sup>1,2</sup>, Sergey  
5 Korkin<sup>1,2</sup>, Ralph Kahn<sup>2,4</sup>, Jeffrey S. Reid<sup>5</sup>, Edward J. Hyer<sup>5</sup>, Thomas F. Eck<sup>1,2</sup>, Mian Chin<sup>2</sup>, David  
6 J. Diner<sup>6</sup>, Olga Kalashnikova<sup>6</sup>, Oleg Dubovik<sup>7</sup>, Jhoon Kim<sup>8</sup>, Hans Moosmüller<sup>9</sup>

7  
8 <sup>1</sup>Goddard Earth Sciences Technology and Research (GESTAR) II, University of Maryland  
9 Baltimore County, Baltimore, MD, USA

10 <sup>2</sup>NASA Goddard Space Flight Center, Greenbelt, MD, USA

11 <sup>3</sup>NASA Langley Research Center, Hampton, VA, USA

12 <sup>4</sup>Laboratory for Atmospheric and Space Physics, The University of Colorado Boulder, Boulder,  
13 CO, USA

14 <sup>5</sup>US Naval Research Laboratory, Monterey, CA, USA

15 <sup>6</sup>Jet Propulsion Laboratory, California Institute of Technology, Pasadena, CA, USA

16 <sup>7</sup>Laboratoire d'Optique Atmosphérique, Université de Lille-1, CNRS, Villeneuve d'Ascq, France

17 <sup>8</sup>Department of Atmospheric Sciences, Yonsei University, Seoul, Republic of Korea

18 <sup>9</sup>Laboratory for Aerosol Science, Spectroscopy, and Optics, Desert Research Institute, Reno, NV,  
19 USA

20

21 Correspondence to: Myungje Choi (myungje.choi@nasa.gov)

22

23 **Abstract**

24 Wildfires and agricultural burning generate seemingly increasing smoke aerosol emissions,  
25 impacting societal and natural ecosystems. To understand smoke's effects on climate and public  
26 health, we analyzed the spatiotemporal distribution of smoke aerosols, focusing on two major  
27 light-absorbing components, black carbon (BC) and brown carbon (BrC) aerosols. Using NASA's  
28 Earth Polychromatic Imaging Camera (EPIC) instrument aboard the NOAA's Deep Space Climate  
29 Observatory (DSCOVR) spacecraft, we inferred BC and BrC volume fractions and particle mass  
30 concentrations based on spectral absorption provided by the Multi-Angle Implementation of  
31 Atmospheric Correction (MAIAC) algorithm with 1-2 hours temporal resolution and ~10 km  
32 spatial resolution over North America and Central Africa. Our analyses of regional smoke  
33 properties reveal distinct characteristics for aerosol optical depth (AOD) at 443 nm, spectral single  
34 scattering albedo (SSA), aerosol layer height (ALH), and BC and BrC amounts. Smoke cases in  
35 North America show extremely high AOD up to 6, with elevated ALH (6-7 km) and significant  
36 BrC components up to 250 mg/m<sup>2</sup> along the transport paths, whereas the smoke aerosols in Central  
37 Africa exhibited stronger light absorption (i.e., lower SSA) and lower AOD, resulting in higher  
38 BC mass concentrations and similar BrC mass concentrations than the cases in North America.  
39 Seasonal burning source locations in Central Africa following the seasonal shift of Inter Tropical  
40 Convergence Zone and diurnal variations in smoke amounts were also captured. Comparison of  
41 retrieved AOD<sub>443</sub>, SSA<sub>443</sub>, SSA<sub>680</sub>, and ALH with collocated AERONET and CALIOP  
42 measurements shows agreement with *rmse* of 0.2, 0.03-0.04, 0.02-0.04, and 0.8-1.3 km,  
43 respectively. Analysis of spatiotemporally average reveals distinct geographical characteristics in  
44 smoke properties closely linked to burning types and meteorological conditions. Forest wildfires  
45 over western North America generated smoke with small BC volume fraction of 0.011 and high  
46 ALH with large variability ( $2.2 \pm 1.2$  km), whereas smoke from wildfires and agricultural burning  
47 over Mexico region shows more absorption and low ALH. Smoke from savanna fires over Central  
48 Africa has the most absorption with high BC volume fraction (0.015) and low ALH with small  
49 variation ( $1.8 \pm 0.6$  km) among the analyzed regions. Tropical forest smoke was less absorbing  
50 and had a high variance in ALH. We also quantify the estimation uncertainties related to the  
51 assumptions of BC and BrC refractive indices. The MAIAC EPIC smoke properties with BC and  
52 BrC volume and mass fractions and assessment of layer height provide observational constraints  
53 for radiative forcing modeling and air quality and health studies.

54  
55 **Keywords:** EPIC, light absorbing smoke aerosol component, BC, BrC

56

## 57 **1. Introduction**

58 Natural and anthropogenic fires affect and shape nearly every terrestrial vegetated  
59 ecosystem on the planet (Pausas and Keeley, 2009; Bond and Keeley, 2005), and their emissions  
60 have long been known to affect the global atmospheric composition and radiative budget (Hobbs  
61 et al., 1997; Seiler and Crutzen, 1980). Recent climate changes and anthropogenic activities have  
62 affected wildfire and agricultural fire occurrence in many regions (Liu et al., 2010; Dennison et  
63 al., 2014). Global monitoring of atmospheric smoke aerosol chemical, optical, and microphysical  
64 properties is important to quantify the impacts of increasing biomass burning on climate and air  
65 quality. However, the current understanding of smoke aerosol radiative forcing is still insufficient  
66 due to its high spatiotemporal variability in combination with the dynamic nature of smoke and  
67 variability of its physical and optical properties (IPCC, 2023).

68 One characteristic that distinguishes smoke particle components from other components is  
69 light absorption. Absorbing particle components converting incident electromagnetic energy into  
70 thermal energy results in heating of both the particles and the ambient surrounding atmosphere.  
71 Aerosol light absorption greatly affects direct radiative forcing and atmospheric stability and  
72 convections (IPCC, 2023; Bellouin et al., 2005; Yu et al., 2002). Smoke particles emitted from  
73 biomass burning typically contain two major light-absorbing carbonaceous components: black  
74 carbon (BC) and brown carbon (BrC). The proportions of these light-absorbing components and  
75 their mixing ratios determine the spectral absorption characteristics (e.g., Jacobson, 2001;  
76 Chakrabarty et al., 2023).

77 BC is a byproduct of the incomplete combustion of carbonaceous materials. There is no  
78 specific chemical makeup of BC and depending on measurement techniques it is also called soot,  
79 elemental carbon, or light-absorbing carbon (Reid et al., 2005a; Moosmüller et al., 2009; Andreae  
80 and Gelencsér, 2006). BC is visibly black, resulting in a high and spectrally invariant imaginary  
81 refractive index ( $\sim 0.79$ ) across UV-visible wavelengths (Bond and Bergstrom, 2006). During  
82 combustion, tiny BC spherules are aggregated with each other and grow by absorbing surrounding  
83 gas-phase molecules into large particles with a complex, generally fractal-like morphology  
84 (Moosmüller et al., 2009). Emitted atmospheric BC particles are generally hydrophobic (Petters et  
85 al., 2009), but can quickly evolve to hydrophilic if they acquire water-soluble coatings upon  
86 emission or during atmospheric aging (Tritscher et al., 2011). Atmospheric aging processes change  
87 BC's physical and chemical particle structure (Corbin et al., 2023; Bhandari et al., 2019; Sengupta  
88 et al., 2020), as well as optical properties (Gyawali et al., 2017; Kleinman et al., 2020; Reid et al.,  
89 2005b). Particle evolutions combine with the high spatial and temporal variability of the sources  
90 to make the net radiative effects of these particles highly uncertain (Bond et al., 2013; IPCC, 2023;  
91 Chakrabarty et al., 2023).

92 The largest carbonaceous aerosol component directly emitted from biomass burning is  
93 organic carbon (OC; e.g., Andreae and Merlet, 2001; Andreae, 2019 and references therein). This  
94 study defines the OC with significant light absorbing property in the tropospheric solar spectrum  
95 as brown carbon (BrC; e.g., Laskin et al., 2015). BrC exhibits spectral variability, absorbing more  
96 ultraviolet (UV) and short visible light than long visible light, resulting in a reddish or brownish

97 appearance. Its imaginary refractive index varies spectrally, with generally higher values at shorter  
98 (i.e., UV) wavelengths and decreasing toward longer, visible and infrared (IR) wavelengths  
99 (Kirchstetter et al., 2004). BrC emission and the chemical processes responsible for BrC formation  
100 are complex and not yet fully understood. Some studies suggest BrC consists primarily of water-  
101 soluble organic carbon compounds and humic-like substances (Sun et al., 2007; Phillips and Smith,  
102 2014; Hoffer et al., 2006) whereas others suggest that non-polar compounds can absorb more light  
103 than polar compounds, especially in the UV and short-wavelength visible (Sengupta et al., 2018).  
104 BrC compounds can be released from smoldering biomass burning or formed through secondary  
105 organic aerosol processes in the atmosphere (Chakrabarty et al., 2010; Laskin et al., 2015). BC  
106 coated with non-absorbing organic and inorganic may exhibit a similar wavelength dependence of  
107 absorption, with higher values at shorter wavelengths (Wang et al., 2016). This similarity makes  
108 it challenging to differentiate between BrC and coated BC based on spectral absorption alone.  
109 Therefore, our "BrC" results may include contributions from coated BC.

110 According to the latest Intergovernmental Panel on Climate Change (IPCC) report (IPCC,  
111 2023), the present day global effective radiative forcing of black carbon from fossil fuel and biofuel  
112 is estimated at  $0.107 \text{ W m}^{-2}$  with a 5-95% uncertainty range of  $-0.202$  to  $0.417 \text{ W m}^{-2}$ , with  
113 respect to the pre-industrial time of 1750. In contrast, primary organic aerosols from fossil fuel  
114 and biofuel, related to OC, exhibit a cooling effect of  $-0.209 \text{ W m}^{-2}$ , with an uncertainty range of  
115  $-0.439$  to  $-0.021 \text{ W m}^{-2}$ . Although BrC is not directly considered in this assessment, its radiative  
116 forcing is partially accounted for within primary organic aerosol, biomass burning, or secondary  
117 organic aerosols in some global aerosol models. Combining ground-based measurements and  
118 chemical transport modeling, Jo et al. (2016) attributed non-BC absorption to BrC and estimated  
119 BrC fraction as 21% of the global mean surface OC concentration, significantly impacting ozone  
120 photochemistry by altering the UV radiation field. Zhang et al. (2020) estimated that the global  
121 BrC direct radiative effect is  $0.10 \text{ W m}^{-2}$ , suggesting that BrC can heat the tropical mid and upper  
122 troposphere more than BC. Still, much uncertainty remains about BrC due to limited measurements  
123 and the complex processes involved, challenging accurate estimates of its radiative impact on  
124 climate (Liu et al., 2020).

125 Intensive *in situ* measurements have been instrumental in identifying the composition-  
126 related spectral light-absorption properties of smoke plumes, as summarized in Bond and  
127 Bergstrom (2006), Andreae and Gelencsér (2006), Moosmüller et al. (2009), and Samset et al.  
128 (2018). These measurements have enabled remote sensing techniques to differentiate between  
129 various light-absorbing components in smoke plumes. For example, the Aerosol Robotic Network  
130 (AERONET) sunphotometers routinely provide aerosol optical and microphysical properties,  
131 including spectral refractive indices from many sites worldwide (Holben et al., 1998; Dubovik and  
132 King, 2000). Using AERONET inversion data, Schuster et al. (2016) inferred aerosol components  
133 over smoke- and dust-dominated regions by matching AERONET spectral refractive index to  
134 mixtures of components with different assumed optical properties. Specific absorbing components  
135 were assumed as inclusions: BC and BrC for smoke and iron oxides of hematite and goethite for  
136 dust aerosols. Wang et al. (2013) and Choi et al. (2020) applied a similar approach to East Asia

137 sites. The synergy between visible/near-IR AERONET measurement and UV/visible multifilter  
138 rotating shadowband radiometer (MFRSR) measurements confirmed the sensitivity of spectral  
139 absorption consistent with a BrC component (Mok et al., 2016, 2018).

140         Inferring aerosol composition from satellites is more challenging than from ground-based  
141 remote sensing due to the need to account for the surface contribution to the top-of-atmosphere  
142 signal, and the much greater range of conditions that space-borne instrument samples. Retrieving  
143 aerosol absorptions using multi-spectral bands in near UV wavelengths has been applied to  
144 instruments such as the Total Ozone Mapping Spectrometer (TOMS) and the Ozone Monitoring  
145 Instrument (OMI), which have data records spanning decades, as well as more recently launched  
146 instruments like the TROPOspheric Monitoring Instrument (TROPOMI) and Earth Polychromatic  
147 Imaging Camera (EPIC; Torres et al., 1998, 2007, 2013, 2020; Ahn et al., 2021). The fraction of  
148 retrieved single scattering albedo (SSA) within the expected error, defined as a fraction within  
149  $\pm 0.03$  from AERONET SSA, is approximately 50%, based on long-term and global validation  
150 across these sensors (Ahn et al., 2021; Torres et al., 2020).

151         The Generalized Retrieval of Aerosol and Surface Properties (GRASP) algorithm  
152 (Dubovik et al., 2011, 2014) utilizes the multi-angle, multi-channel, and both radiometric and  
153 polarimetric measurements from the POLarization and Directionality of the Earth's Reflectances  
154 (POLDER) instruments. With increased information incorporated by a multi-pixel multi-temporal  
155 smoothness constraint, the GRASP algorithm retrieves aerosol optical depth (AOD), particle size  
156 information, and absorption, showing robust agreement with global AERONET measurements  
157 (Chen et al., 2020). Recent improvement of the GRASP algorithm included the direct estimation  
158 of aerosol chemical composition concentrations without the need for intermediate steps such as  
159 retrieving refractive indices and particle size distributions (Li et al., 2019, 2020). The Multi-angle  
160 Imaging SpectroRadiometer (MISR) research algorithm also accounts for black-smoke and brown-  
161 smoke aerosol models (Limbacher et al., 2022), analogous to the BC and BrC components in this  
162 study, and is utilized to analyze fractional AODs along transport paths (Junghenn Noyes et al.,  
163 2020a, b, 2022). Still, it is worth noting that POLDER and MISR measurements are limited to  
164 visible and near-infrared (NIR) channels and do not include ultraviolet (UV) channels, where  
165 spectral absorption due to BC and in particular BrC is more pronounced.

166         The EPIC sensor aboard the Deep Space Climate Observatory (DSCOVR) spacecraft has  
167 provided UV-near IR measurements of Earth since 2015 (Marshak et al., 2018). Recent studies by  
168 (Lyapustin et al., 2021b) have utilized the Multi-Angle Implementation of Atmospheric Correction  
169 (MAIAC) processing of EPIC measurements to derive AOD and spectral absorption. It enables  
170 inferring aerosol chemical compositional differences, such as BC and BrC in smoke aerosol  
171 plumes and iron oxides (e.g., hematite and goethite) in dust aerosol plumes. DSCOVR's orbit  
172 around the Lagrange-1 point, where the spacecraft remains stably positioned between the sun and  
173 Earth, allows for global monitoring multiple times per day during the daylight time with a temporal  
174 resolution of 1-2 hours. In our study, we used EPIC measurements to infer BC and BrC volume  
175 fractions and mass concentrations in smoke plumes and identified distinct smoke properties over

176 North America and Central Africa. The estimation of iron oxides in dust aerosols using the MAIAC  
177 EPIC product was addressed in Go et al. (2022).

178 The structure of the paper is as follows. Section 2 introduces the MAIAC EPIC smoke  
179 aerosol retrieval algorithm and describes the methodology for inferring BC and BrC volume  
180 fractions and mass concentrations. It also includes descriptions of study regions and of AERONET  
181 and CALIOP validation datasets. In Section 3, we analyzed individual smoke cases over North  
182 America and Central Africa, and provided validation of AOD, spectral SSA, and aerosol layer  
183 height (ALH). Additionally, time-integrated regional properties, including BrC/BC ratios, and  
184 uncertainty estimates based on different inclusion assumptions are discussed. Finally, Section 4  
185 offers summary and concluding remarks.

## 186 2. Data and methods

### 187 2.1 MAIAC EPIC processing algorithm

188 EPIC measurements cover the entire sunlit hemisphere of Earth with ten narrowband  
189 spectral channels from 317.5 to 779.5 nm. The spatial resolution of EPIC is ~8-16 km at nadir,  
190 degrading toward the edge of the image. MAIAC EPIC algorithm grids and processes L1B data at  
191 10 km resolution providing an oversampling. DSCOVR's Lagrange point 1 orbit between the Earth  
192 and the Sun (~1.5 million kilometers) enables global multi-temporal daytime measurements, with  
193 10–12 observations in boreal summer and 6-7 observations in winter at mid-latitudes and little  
194 seasonal change in tropical latitudes. Detailed information on EPIC measurements can be found  
195 in Marshak et al. (2018). Following the MAIAC Moderate Resolution Imaging Spectroradiometer  
196 (MODIS) algorithm (Lyapustin et al., 2018), the standard MAIAC processing offers cloud  
197 detection, atmospheric correction, and AOD with regionally specified background aerosol models  
198 ("background AOD"; Lyapustin et al., 2021a). In addition, a newly developed absorbing smoke or  
199 dust aerosol retrieval process was applied to both land and ocean pixels. Smoke/dust detection and  
200 separation are based on various tests including UV aerosol index and spectral AOD shape. As  
201 EPIC band configuration does not allow to distinguish between smoke and dust aerosols, the dust  
202 retrievals are only performed over pre-defined dust regions whereas smoke retrievals are  
203 performed elsewhere globally (Lyapustin et al., 2021b).

204 The full algorithm description will be given elsewhere; here we provide a very brief  
205 overview to facilitate understanding of our results. The novel version 3 (v3) MAIAC algorithm  
206 represents spectral aerosol absorption with two parameters, the imaginary refractive index at 680  
207 nm ( $k_0$ ) and spectral absorption exponent (SAE), using a conventional power-law expression,  $k_\lambda =$   
208  $k_0(\lambda/\lambda_0)^{-SAE}$  where  $\lambda_0 = 680$  nm. The real refractive index is assumed to have a spectrally  
209 invariant value of 1.51 (Lyapustin et al., 2021b). The particle log-normal volume size distribution

210 is defined as  $\frac{dV(r)}{d\ln(r)} = \sum_{i=1}^2 \frac{c_{v,i}}{\sqrt{2\pi}\sigma_i} e^{-\frac{1}{2}\left(\frac{\ln(r)-\ln(r_{v,i})}{\sigma_i}\right)^2}$ , where  $i$  indicates each mode (fine and coarse),

211  $r$  is the particle radius,  $r_{v,i}$  is the volume mean radius,  $\sigma_i$  is the geometric standard deviation,  $c_{v,i}$

212 is the volumetric concentration. For smoke aerosols, we assumed fine mode volume mean radius  
213 (0.14  $\mu\text{m}$ ) and geometric standard deviation (0.4  $\mu\text{m}$ ), coarse mode volumetric mean radius (2.8  
214  $\mu\text{m}$ ) and geometric standard deviation (0.6  $\mu\text{m}$ ). In MAIAC v3, the Levenberg-Marquardt  
215 nonlinear optimal fitting algorithm (Levenberg, 1944; Marquardt, 1963) is used to simultaneously  
216 retrieve four parameters {AOD<sub>443</sub>,  $k_0$ , SAE, ALH} by matching EPIC measurements at UV to NIR  
217 wavelengths, including oxygen A and B bands. The algorithm uses pre-computed look-up tables  
218 (LUTs) covering the full range of expected variability of the above parameters. The maximum  
219 value of AOD at 443 nm in the algorithm is set to 6. Vertically, the aerosol is modeled by a single  
220 2 km-thick aerosol layer placed at different altitudes in the atmosphere, and the reported ALH is  
221 defined as the midpoint height of the layer. To avoid systemic biases in absorption, this retrieval  
222 is performed over detected absorbing smoke/dust pixels when the retrieved AOD, based on the  
223 background aerosol model with fixed regional properties, is greater than 0.4. Note that although  
224 smoke retrievals are limited with “background AOD<sub>443</sub> > 0.4” the retrieved smoke AOD<sub>443</sub> could  
225 be lower than 0.4 due to different assumption of microphysical properties and simultaneous  
226 retrieval of spectral absorption and ALH.

## 227 **2.2 MAIAC smoke composition inference**

228         Given a very different spectral absorption of BC (high and spectrally fairly flat) and BrC  
229 (low and strongly increasing towards UV), the retrieved spectral absorption can be used to derive  
230 fractions of absorbing components. We assume that smoke aerosols consist of a non-absorbing  
231 host and two absorbing species, BC and BrC, with internal mixing based on Maxwell Garnett  
232 effective medium approximation (MG-EMA) (Bohren and Huffman, 1998; Schuster et al., 2005,  
233 2016). The MG-EMA is suitable for characterizing smoke particles and is computationally  
234 efficient (Garnett, 1904; Bohren and Huffman, 1998; Schuster et al., 2005; Markel, 2016a, b). For  
235 that reason, it is widely used for inferring aerosol compositions from ground-based or satellite-  
236 based remote sensing (Li et al., 2019; Schuster et al., 2005, 2016; Choi et al., 2020; Go et al., 2022).  
237 Studies showed that different internal mixing rules, such as Bruggeman approximation or volume  
238 averaging, yields similar results to the MG-EMA for inferring smoke components (Schuster et al.,  
239 2016; Li et al., 2019; and references therein). External mixing could be assumed, resulting in lower  
240 absorption than internal mixing (Lesins et al., 2002; Lack et al., 2012), but most BC particles exist  
241 internally mixed with other components in biomass burning plumes (Schwarz et al., 2008). The  
242 non-absorbing host (or medium) represents a mixture of non-absorbing or low-absorbing  
243 components in smoke, such as non-absorbing OC, sulfate, nitrate, and/or ammonium. Although  
244 there are various ranges of refractive indices for both BC and BrC based on literature and  
245 experiments, this study assumes fixed refractive index to estimate their fractions from the limited  
246 information of the retrieved optical properties. The BC refractive index assumes Bond and  
247 Bergstrom (2006)’s suggestion of spectrally flat with a real part ( $n$ ) of 1.95 and an imaginary part  
248 ( $k$ ) of 0.79 for the visible spectrum (i.e., 400 – 700 nm). Spectral dependence of  $k$  for BrC is based  
249 on Kirchstetter et al. (2004), whereas a constant real part of 1.54 was assumed based on Li et al.  
250 (2019). For a spectrally flat and non-absorbing host we assume  $n=1.51$ , consistent with the smoke

251 aerosol model in the MAIAC EPIC algorithm, and  $k=10^{-9}$  based on Kalashnikova et al. (2018).  
 252 Table 1 summarizes the spectral refractive indices of BC, BrC and host. Please note that a  
 253 sensitivity test for different assumptions regarding BC and BrC imaginary refractive indices  
 254 affecting their volume fractions is detailed in Sec 3.5.

255  
 256 Table 1. Spectral refractive indices of smoke aerosol components at EPIC wavelengths.

Wavelengths (nm)	BC		BrC		host	
	n	k	n	k	n	k
340	1.95	0.790	1.54	0.187	1.51	$10^{-9}$
388	1.95	0.790	1.54	0.125	1.51	$10^{-9}$
443	1.95	0.790	1.54	0.070	1.51	$10^{-9}$
680	1.95	0.790	1.54	0.003	1.51	$10^{-9}$

257  
 258 The MG-EMA equation for smoke aerosol mixtures, as described in Bohren and Huffman  
 259 (1998) and Schuster et al., (2005), is presented below.

$$260 \quad \epsilon_m = \epsilon_h \left[ 1 + \frac{3 \left( f_{BC} \frac{\epsilon_{BC} - \epsilon_h}{\epsilon_{BC} + 2\epsilon_h} + f_{BrC} \frac{\epsilon_{BrC} - \epsilon_h}{\epsilon_{BrC} + 2\epsilon_h} \right)}{1 - f_{BC} \frac{\epsilon_{BC} - \epsilon_h}{\epsilon_{BC} + 2\epsilon_h} - f_{BrC} \frac{\epsilon_{BrC} - \epsilon_h}{\epsilon_{BrC} + 2\epsilon_h}} \right]$$

261 Here,  $\epsilon_m$ ,  $\epsilon_h$ ,  $\epsilon_{BC}$ , and  $\epsilon_{BrC}$  represent the complex dielectric functions of the mixture, host,  
 262 BC, and BrC, respectively, and  $f_{BC}$  and  $f_{BrC}$  denote the volume fractions of BC and BrC,  
 263 respectively. Note that identical BC and BrC components are assumed for both fine and coarse  
 264 modes. Throughout plume evolution, different processes such as oxidation, hydration, deposition  
 265 of volatile organics onto existing particles, or new particle formation, may lead to larger particle  
 266 sizes. Consequently, the fine-mode and coarse-mode components in smoke aerosols could exhibit  
 267 differences. Schuster et al. (2016) also accounted for different component combinations between  
 268 fine and coarse modes, considering dust particles for the coarse mode. It should be noted that  
 269 biomass burning aerosols are strongly dominated by the fine mode component, with typically only  
 270 a minor coarse mode AOD. However, the MAIAC EPIC processing relies on a static particle size  
 271 distribution, and dynamic separation of fine and coarse modes is challenging with limited  
 272 measurement information.

273 The refractive indices of the mixture can be determined using the following equations:

$$274 \quad n = \sqrt{\frac{\sqrt{\epsilon_r^2 + \epsilon_i^2} + \epsilon_r}{2}},$$

$$275 \quad k = \sqrt{\frac{\sqrt{\epsilon_r^2 + \epsilon_i^2} - \epsilon_r}{2}},$$



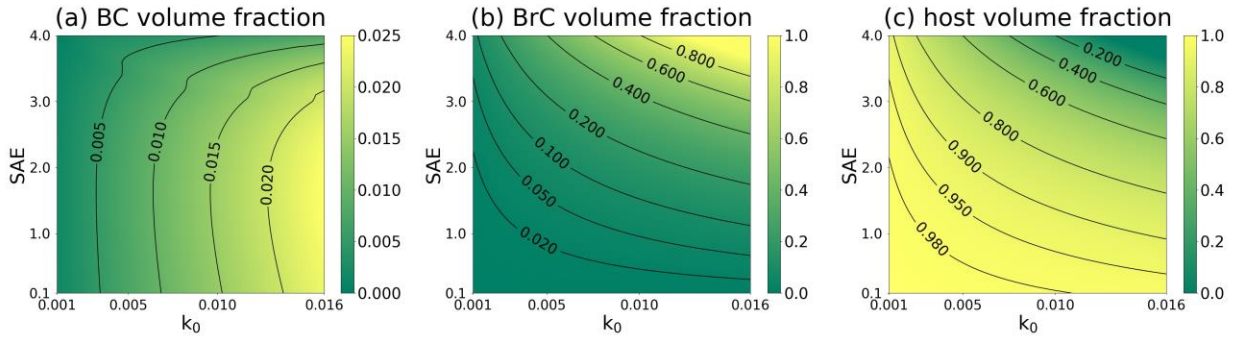
276 where  $\epsilon_r$  and  $\epsilon_i$  represent the real and imaginary parts of the mixture dielectric function  $\epsilon_m$ . Given  
 277 fixed spectral refractive indices of the host and inclusions (BC and BrC), the mixture refractive  
 278 indices are determined by the volume fractions of two inclusions ( $f_{BC}$  and  $f_{BrC}$ ).

279 Subsequently, we utilized the Levenberg-Marquardt nonlinear least-square fitting method  
 280 (Levenberg, 1944; Marquardt, 1963; Press et al., 2007) to derive the volume fractions of inclusions  
 281 by comparing inferred and calculated refractive indices with the MG-EMA. Retrieved  $k_0$  and SAE  
 282 were converted into spectral imaginary refractive indices ( $k_\lambda$  for  $\lambda$  of 340, 380, 443, and 680 nm)  
 283 and matched with theoretical values of a mixture to find solutions for  $f_{BC}$  and  $f_{BrC}$ .

284 Fig. 1 illustrates the derivable BC, BrC, and host volume fractions for assumed ranges of  
 285  $k_0$  (0.001–0.016) and SAE (0.1–4) in the MAIAC EPIC algorithm. Available  $f_{BC}$ ,  $f_{BrC}$ , and  $f_{host}$   
 286 ranges are from 0 to 0.025, 0.994, and 0.998, respectively, where  $f_{host} = 1 - f_{BC} - f_{BrC}$ . The  
 287 maximum  $f_{BC}$  of 0.025 can be found in the condition of maximum  $k_0$  of 0.016. A high  $f_{BrC}$  near  
 288 one can be retrieved when both  $k_0$  and SAE are high. The host volume fraction ( $f_{host}$ ) shows an  
 289 opposite tendency to  $f_{BrC}$  and is low when both  $k_0$  and SAE are high. Conversion from retrieved  
 290  $k_0$  and SAE to volume fractions follows the presented distributions.

291 It should be mentioned that the upper limit of  $k_0=0.016$  was found empirically based on  
 292 limited EPIC regional processing, and then confirmed by the global processing of EPIC data.  
 293 However, this limit may be increased in the future based on detailed analysis of EPIC retrievals,  
 294 in particular because AERONET inversion retrievals often show higher values, for example in  
 295 Central and southern Africa savanna burning region (Eck et al., 2003).

296



297  
 298 Figure 1. The range of volume fractions for (a) BC, (b) BrC, and (c) host across different values  
 299 of  $k_0$  and SAE.

300

301 The inferred volume fractions of BC and BrC can be converted to column-integrated  
 302 volume concentrations as,

303

$$C_V = C_{Vf} + C_{Vc} = \frac{AOD_f}{h_f} + \frac{AOD_c}{h_c},$$

304

$$AOD_f = AOD \cdot \left( \frac{C_{Vf}}{C_{Vf} + C_{Vc}} \right),$$

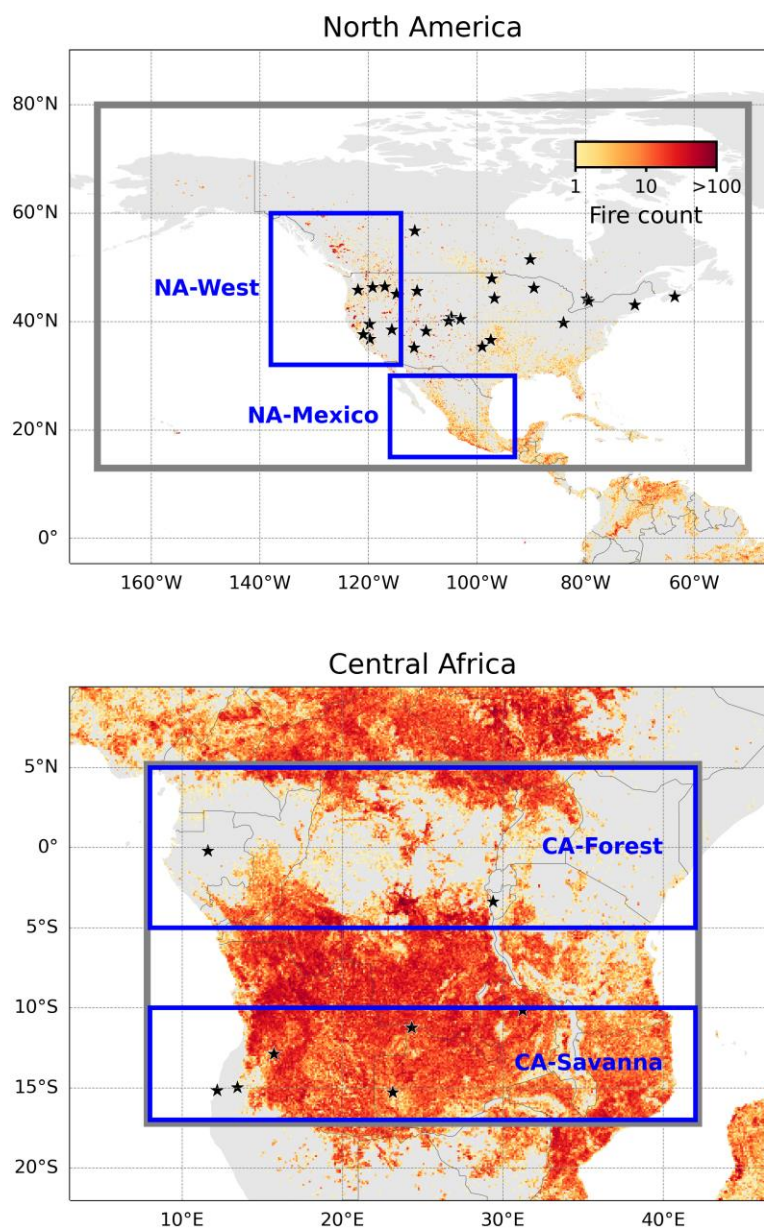
305

$$AOD_c = AOD \cdot \left( \frac{C_{Vc}}{C_{Vf} + C_{Vc}} \right),$$

306 where  $C_V$  is the column-integrated volume concentration with a unit of  $\mu\text{m}^3/\mu\text{m}^2$ , the subscripts  $f$   
307 and  $c$  indicate fine-mode and coarse-mode, respectively. Despite the regional dependence of  $\frac{C_{Vc}}{C_{Vf}}$   
308 in the 4D-retrieval algorithm for smoke, we assume a static  $\frac{C_{Vc}}{C_{Vf}}$  of 0.7 for BC and BrC processing  
309 to maintain consistency and reduce regional discrepancies arising from the ratio. Hygroscopicity  
310 was neglected by using a static AOD per volume concentration regardless of relative humidity.  
311 Given the size distribution and  $n$ ,  $h_f$  of  $8.43 \mu\text{m}^2/\mu\text{m}^3$  is fine mode  $\text{AOD}_{443}$  per unit volume  
312 concentration ( $\mu\text{m}^3/\mu\text{m}^2$ ) and  $h_c$  of  $0.72 \mu\text{m}^2/\mu\text{m}^3$  is coarse mode  $\text{AOD}_{443}$  per unit volume  
313 concentration, as calculated based on Mie theory in the MAIC EPIC smoke model (Lyapustin et  
314 al., 2021b). Given the complex refractive indices, size distribution with fine-mode or coarse-mode  
315 only, and non-sphericity, the  $h$  values, representing total column AOD per unit volume  
316 concentration, are computed using the DLS (sphere and spheroid) model (Dubovik et al., 2006) at  
317 volume concentration of  $1 \mu\text{m}^3/\mu\text{m}^2$ .  $h_f$  and  $h_c$  are computed separately for the fine and coarse  
318 modes within the MAIAC look-up table generation package and can be used to assess mass  
319 extinction efficiency (MEE) with assumption of particle density. The column-integrated mass  
320 concentration of the chemical component is calculated as  $C_{M,i} = C_V \cdot f_i \cdot \rho_i$ , where  $i$  indicates  
321 inclusions (BC and BrC) and  $\rho$  is mass concentration per unit volume. We use  $\rho_{\text{BC}}$  of  $1.8 \text{ g/cm}^3$   
322 and  $\rho_{\text{BrC}}$  of  $1.2 \text{ g/cm}^3$  following previous studies (Bond and Bergstrom, 2006; Turpin and Lim,  
323 2001; Schuster et al., 2016; Li et al., 2020).

### 324 2.3 Study regions

325 We selected two major regions where smoke aerosols are dominant but exhibit different  
326 characteristics: North America ( $170^\circ\text{W}$ - $50^\circ\text{W}$  and  $13^\circ\text{N}$ - $80^\circ\text{N}$ ) and Central Africa ( $8^\circ\text{E}$ - $42^\circ\text{E}$  and  
327  $17^\circ\text{S}$ - $5^\circ\text{N}$ ). To avoid potential interference from dust aerosols on smoke analysis, we excluded the  
328 Sahel region bounding the Sahara Desert from this study. The selected smoke aerosol analysis  
329 regions, along with detected fire counts from the Visible Infrared Imaging Radiometer Suite  
330 (VIIRS) instrument onboard the Suomi National Polar-orbiting Partnership (SNPP) satellite in  
331 2018, are presented in Fig 2. This study focused on the entire year of 2018, a year marked by one  
332 of highest monthly average AOD during the summer over North America (Eck et al., 2023). The  
333 EPIC dataset exhibited no temporal gaps, and ample AERONET and CALIOP data were  
334 accessible. Additionally, we included a single case study from 2017 to complement our analysis  
335 over North America.



336  
 337 Figure 2. Cumulative fire detection counts from VIIRS within a 0.1° by 0.1° longitude-latitude  
 338 grid in 2018 over North America and Central Africa. The study regions are denoted by grey  
 339 rectangles, and AERONET locations are marked with blue stars. Subregions including western  
 340 (“NA-West”) and Mexico (“NA-Mexico”) in North America, as well as tropical forest (“CA-  
 341 Forest”) and savanna (“CA-Savanna”) regions in Central Africa are denoted by blue rectangles.

## 342 2.4 AERONET

343 In order to evaluate the EPIC-retrieved AOD and spectral absorption, we utilized the  
 344 Version 3 Level 2.0 AERONET Inversion dataset (Holben et al., 1998; Dubovik and King, 2000;

345 Giles et al., 2019; Sinyuk et al., 2020). The EPIC-retrieved  $AOD_{443}$ ,  $SSA_{443}$  and  $SSA_{680}$  were  
346 compared with the AERONET counterpart derived from direct and sky radiance measurements.  
347 The AERONET measurements of spectral AOD have accuracy of  $\sim 0.01$  to  $0.02$  at optical air mass  
348 of one with higher uncertainty in the UV (Eck et al., 1999). The AERONET retrieved SSA at 440  
349 nm have uncertainty of  $\sim 0.03$  at  $AOD(440)=0.4$  with smaller uncertainties at larger AOD,  
350 decreasing to  $\sim 0.015$  at  $AOD(440)=1.3$  for biomass burning aerosols at the Mongu, Zambia site  
351 (Sinyuk et al., 2020). Spatiotemporal collocation between AERONET and EPIC measurements  
352 was conducted as follows: (1) averaging AERONET AOD within a  $\pm 30$ -min range and averaging  
353 SSA within a  $\pm 3$ -hour range from the EPIC measurement time, and (2) averaging EPIC  $5 \times 5$  pixels  
354 ( $\sim 50 \times 50 \text{ km}^2$ ) collocated with the AERONET sites and limited to cosines of solar zenith angle  
355 and view zenith angle above 0.45 (i.e., solar zenith angle & view zenith angle  $< 63.3^\circ$ ). The EPIC  
356 pixels were spatially averaged when at least 50% of EPIC smoke products are valid in the spatial  
357 window. AERONET retrievals with extinction Ångström exponent between 440 and 675 nm  
358 greater than 0.4 were selected to avoid possible dust contamination. SSA validation was conducted  
359 only when AERONET AOD at 440 nm was greater than 0.6. The AERONET sites with at least  
360 five measurements available were considered. Consequently, a total of 28 and 7 AERONET sites  
361 were chosen over North America and Central Africa, respectively (see Fig 2).

## 362 2.5 CALIOP

363 The Cloud-Aerosol Lidar with Orthogonal Polarization (CALIOP) onboard Cloud-Aerosol  
364 Lidar and Infrared Pathfinder Satellite Observations (CALIPSO) satellite has provided global  
365 measurements of aerosol vertical distribution. We collected profiles of total attenuated backscatter  
366 coefficients at 532 nm ( $\beta$ , unit of  $\text{km}^{-1}\text{sr}^{-1}$ ) from the CALIPSO Lidar Level 2 Aerosol Profile  
367 version 4.51 dataset (“CAL\_LID\_L2\_05kmAPro-Standard-V4-51”) in 2018. Subsequently, we  
368 calculated backscatter-weighted aerosol layer height using the formula  $ALH_{\text{CALIOP}} = \frac{\sum \beta z}{\sum \beta}$ , where  
369  $z$  represents the height of each layer. This definition is widely employed for validating aerosol  
370 layer height using CALIOP (Go et al., 2020; Xu et al., 2019). The  $ALH_{\text{CALIOP}}$  data within a  $\pm 30$   
371 min from EPIC acquisitions were spatially averaged within MAIAC EPIC grid. We used the same  
372 cutoff threshold for the Sun and view zenith angle as above. To mitigate ALH uncertainty for weak  
373 aerosol cases, the ALH comparison was conducted when CALIOP AOD at 532 nm exceeded 0.6.

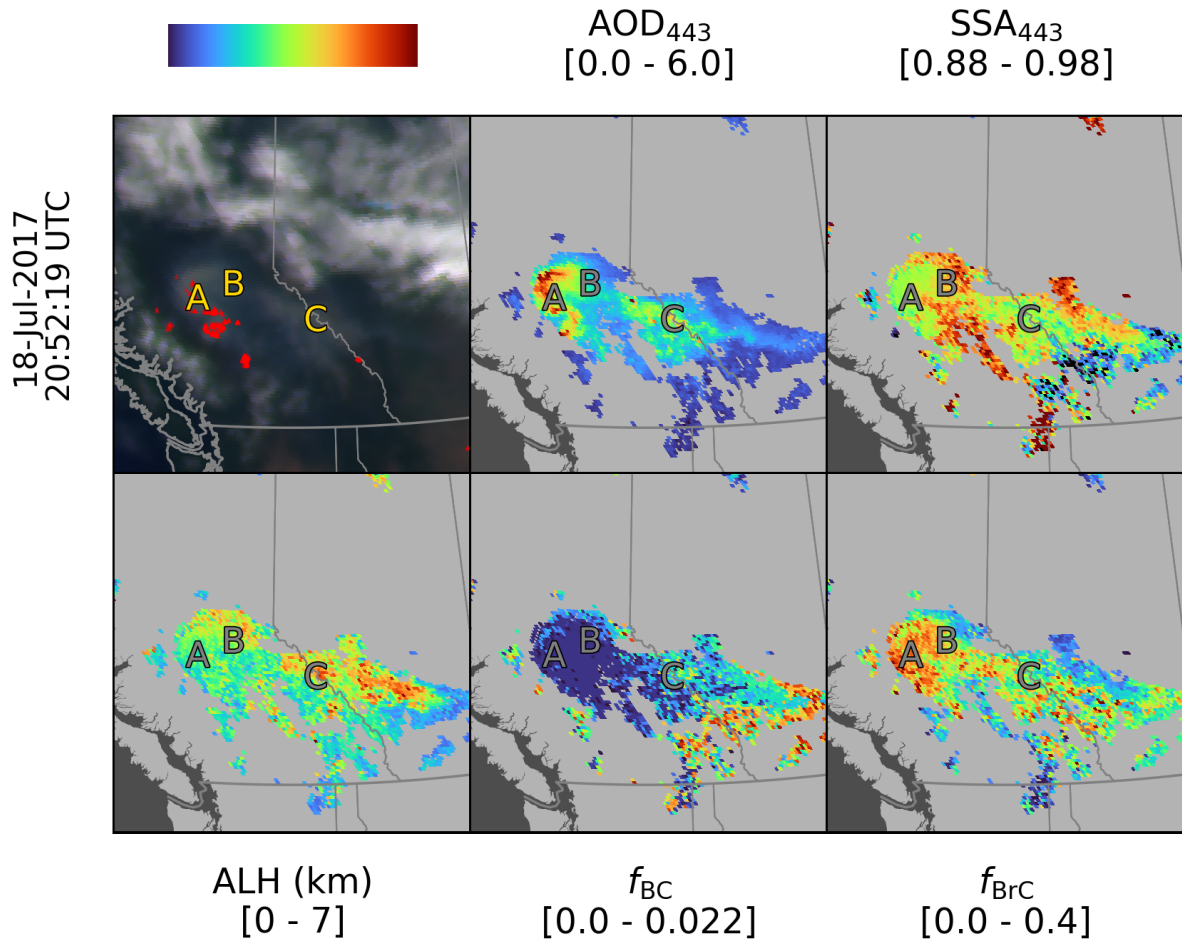
## 374 3. Results

### 375 3.1 Analysis of individual cases

#### 376 3.1.1 North America

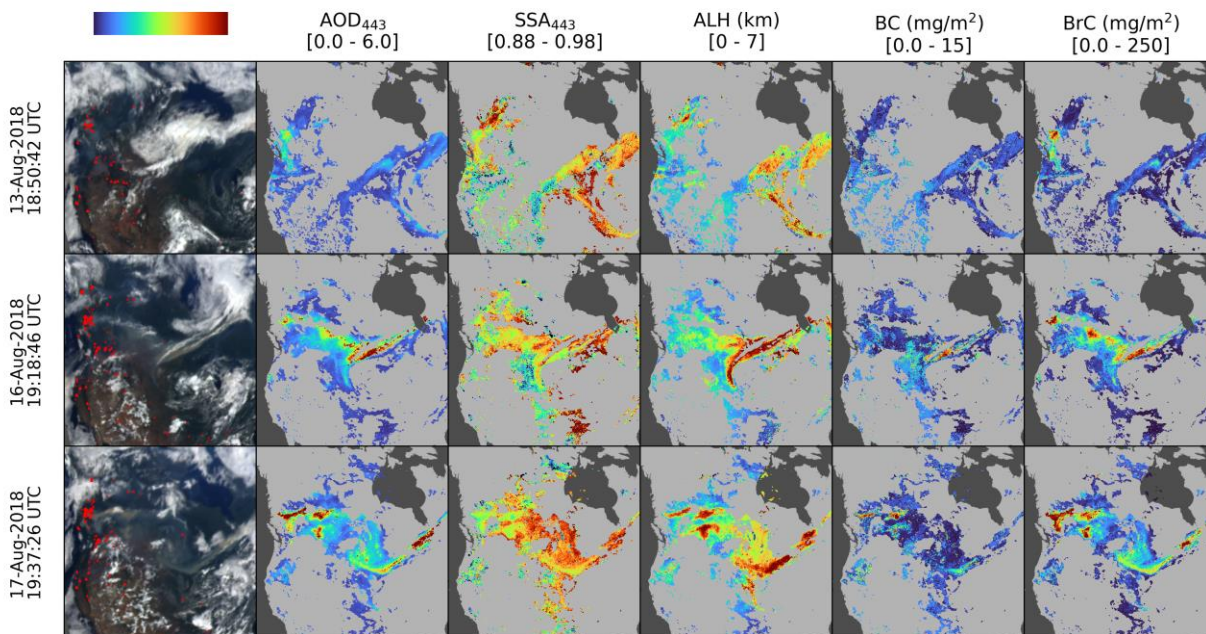
377 Western North America stands out as one of the most active wildfire regions globally. For  
378 our analysis, we selected an intense wildfire and associated smoke aerosol event occurring on July  
379 18, 2017, at 20:52:19 Coordinated Universal Time (UTC) over western Canada in Fig 3. Note that

380 all other analyses in this study are for 2018 except for this case. Utilizing the VIIRS/SNPP Thermal  
381 Anomalies/Fire (Schroeder and Giglio, 2018), visualized as red dots within the true-color images,  
382 we identified wildfires in British Columbia. The true-color image and retrieved smoke particle  
383 properties illustrate the eastward transport of the smoke plume. Specifically, pixels near the  
384 wildfires (region “A” in Fig 3) exhibited  $AOD_{443}$  nearing  $\sim 4-6$ , alongside an  $SSA_{443}$  of  $\sim 0.93$ .  
385 Pixels approximately 50~100 km from the sources (region “B”), show decreased  $AOD_{443}$  ( $\sim 2$ ) and  
386 less absorption ( $SSA_{443}$  of  $\sim 0.96$ ). Notably, the contrast in  $SSA$  is more pronounced at 388 nm  
387 than at 680 nm (not shown). Absorption changes within this distance are related to the aging  
388 process. Freshly emitted particles from wildfires exist in various mixing states and undergo  
389 multiple processes, such as coagulation, condensation/evaporation, oxidation, and secondary  
390 aerosol particles formed from chemical production (Reid et al., 2005a, b; Liu et al., 2020). Smoke  
391 aerosol mixtures become less absorbing in the UV and shortwave visible wavelengths when  
392 transported from sources through these aging processes, consistent with findings from other *in-*  
393 *situ* and remote sensing measurement studies (Junghenn Noyes et al., 2020a, b; Kleinman et al.,  
394 2020). The increased  $SSA_{443}$  from 0.93 to 0.96 (from region “A” to “B”) corresponds to a decrease  
395 in the BrC fraction from 0.3 to 0.1. Aerosol plumes over Alberta, farther downwind to the east  
396 (region “C”), exhibited a) high  $AOD_{443}$  values (1-3), b)  $SSA_{443}$  of  $\sim 0.92-0.94$ , c) increased BC  
397 volume fraction up to 0.01; and d) a similar BrC volume fraction (about 0.3 at the plume center)  
398 for pixels close to the fire sources. The eastern part of the plumes was located farther away from  
399 the source and could have undergone more extensive aging. Smoke aerosol near sources was  
400 located close to the surface (ALH above sea level of  $\sim 1$  km) and was elevated to about 5-6 km in  
401 the downwind area. It is important to consider that the fires could also undergo various stages of  
402 combustion intensity over time, which could also be a factor in BC and BrC production. The  
403 observed differences in ALH suggest that possibly some of these fires were more intense earlier,  
404 leading to the lofting of the plume to 5-6 km. Subsequently, the intensity may have decreased,  
405 resulting in a lower ALH as the plume transitioned to a more smoldering phase. This scenario,  
406 particularly applicable to long plume lengths, implies that fire intensity and the relative combustion  
407 fraction (flaming/smoldering) likely varied over the course of several hours during the transport  
408 of such a long plume distance.



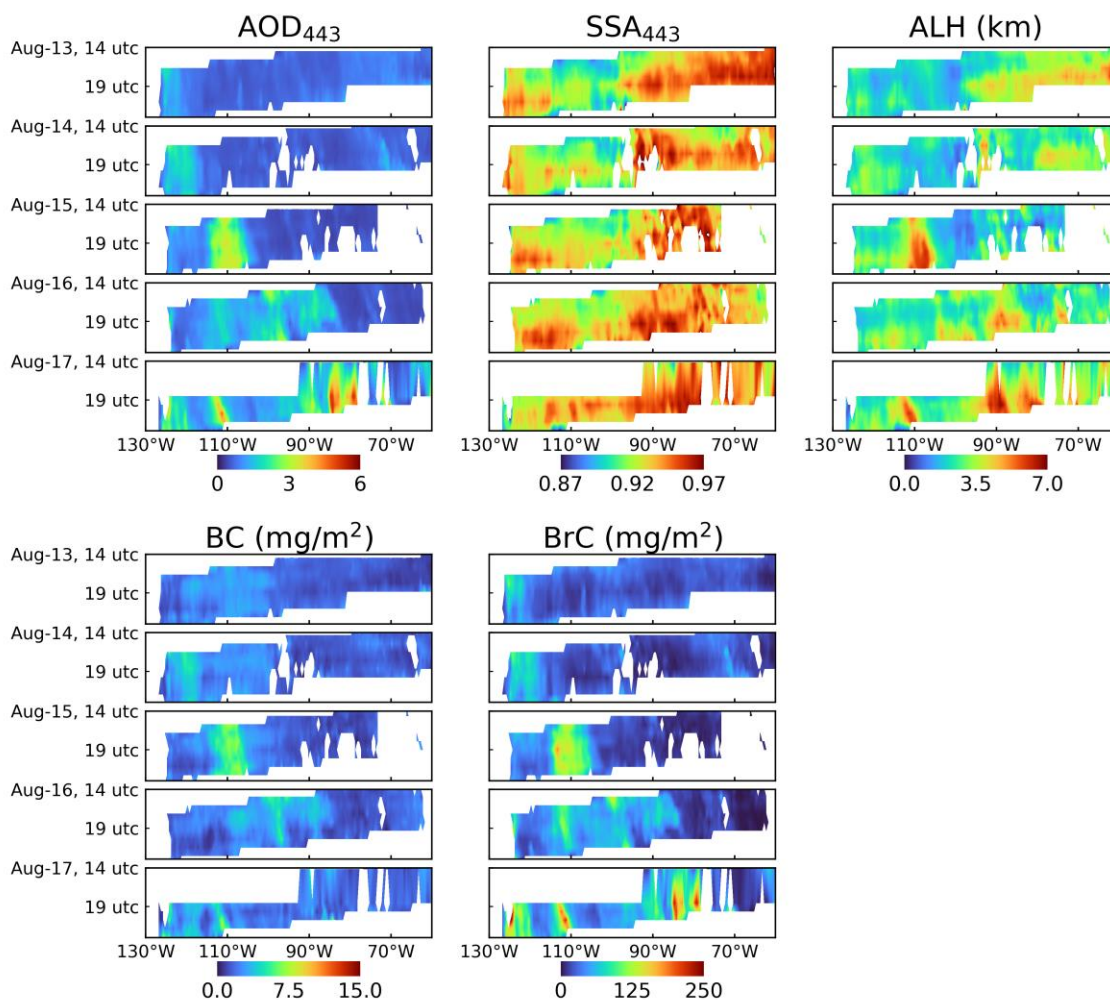
409  
 410 Figure 3. Illustration of EPIC smoke aerosol optical properties over western North America on  
 411 July 18, 2017. Red dots in the first left panel are VIIRS/NPP thermal anomaly hotspots. The  
 412 underlying image and analyses in subsequent panels correspond to EPIC true color and MAIAC  
 413 EPIC retrievals ( $AOD_{443}$ ,  $SSA_{443}$ , and ALH) with inferred BC and BrC volume fractions. The color  
 414 bar scale is indicated at the top of each panel.

415  
 416 Continental-scale smoke aerosol episodes in August 2018, derived from the analysis of  
 417 Lyapustin et al. (2021b), are depicted in Fig 4. On August 13 (top panels), smoke aerosol plumes  
 418 along the west coast of North America, near the detected wildfire sources, exhibit high AOD of  
 419 nearly 3-4 and  $SSA_{443}$  of 0.93 in the plume center. Surrounding pixels of the plume generally show  
 420 lower AOD and higher SSA than the pixels interior to the plume. Subsequently, westerly  
 421 transported plumes with increased AOD (up to ~6) and ALH (~6-7 km) were detected on August  
 422 16 and 17. Corresponding BC and BrC fractions ranged from 0.005 to 0.01 and 0.2 to 0.3 (not  
 423 shown), with column mass concentrations reaching 15 mg/m<sup>2</sup> and 250 mg/m<sup>2</sup>, respectively.



424  
 425 Figure 4. Illustration of smoke aerosol optical properties ( $AOD_{443}$ ,  $SSA_{443}$ , ALH, and BC and BrC  
 426 mass concentrations) over North America on August 13, 16, and 17, 2018. The color bar scale is  
 427 indicated at the top of each panel.

428  
 429 EPIC can effectively monitor the regional-to-continental scale variability of smoke optical  
 430 properties at high temporal cadence. Meridional averages of  $AOD_{443}$ ,  $SSA_{443}$ , ALH, and BC and  
 431 BrC mass concentrations over the period from August 13 to 17, 2018 are represented as Hovmöller  
 432 diagrams in Fig 5. Plume evolution is clearly captured, with a temporal resolution of 1-2 hours,  
 433 from initial smoke aerosol emission over western North America, to subsequent transport toward  
 434 the east with an increased ALH from  $\sim 1$  km to 6-7 km, and eventually to dispersion.



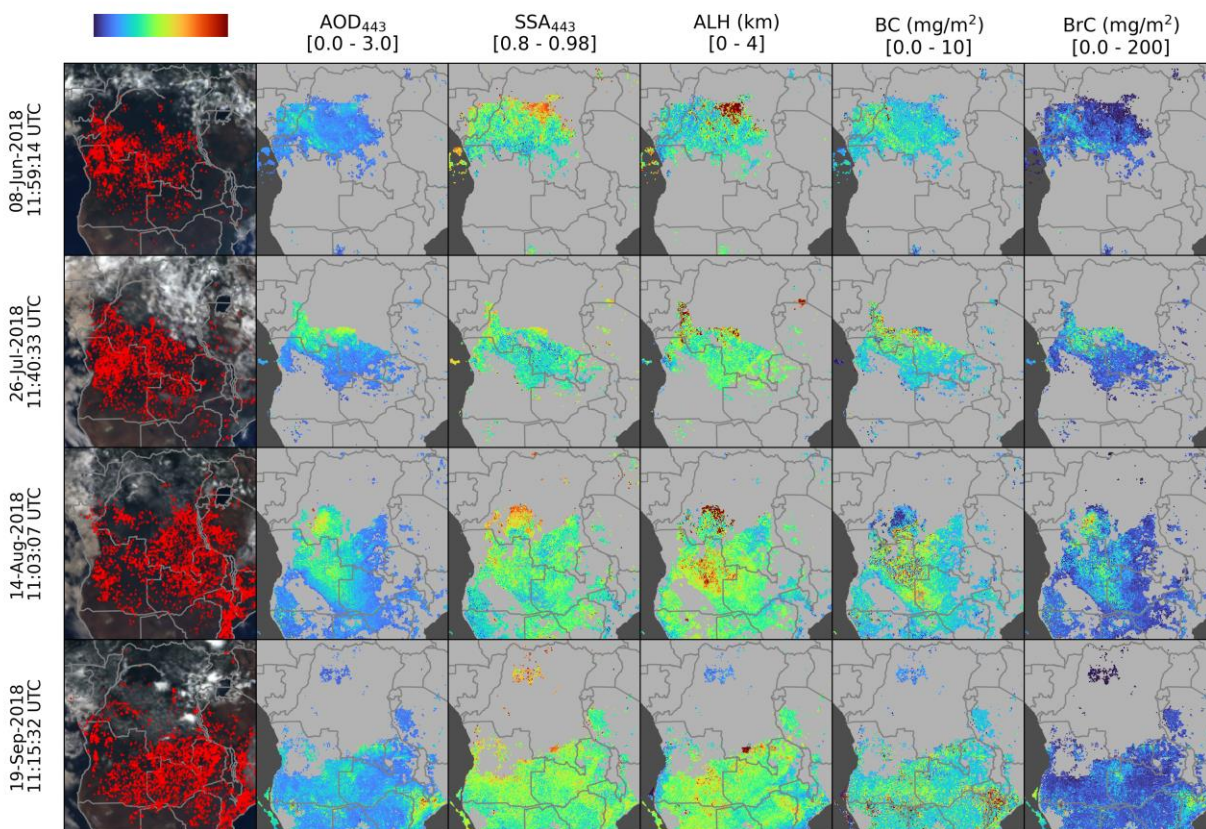
435  
 436 Figure 5. Hovmöller diagrams of AOD<sub>443</sub>, SSA<sub>443</sub>, ALH, and BC and BrC volume fractions over  
 437 North America (130-60°W, 25-53°N, 0.5° longitudinal interval) from August 13 to 17, 2018. Gaps  
 438 in the data are due to low AOD or meteorological clouds.

### 439 3.1.2 Central Africa

440 Biomass burning over Central Africa generates smoke aerosols with distinct optical  
 441 properties. Long-term AERONET measurements over Southern Africa savanna regions indicate  
 442 the strongest absorption among global smoke regions, with SSA values at 440 and 680 nm of 0.87  
 443 and 0.86, respectively (Dubovik et al., 2002; Giles et al., 2012; Sayer et al., 2014). The biomass  
 444 burning emission pattern in Africa follows a clearly defined seasonal cycle, influenced by  
 445 precipitation linked to the seasonal movement of the Inter-Tropical Convergence Zone (ITCZ)  
 446 (Swap et al., 2003). There exists a strong temporal cycle of SSA as well, with the lowest SSA  
 447 values in June due to savanna burning, and increasing through October as more forested areas burn



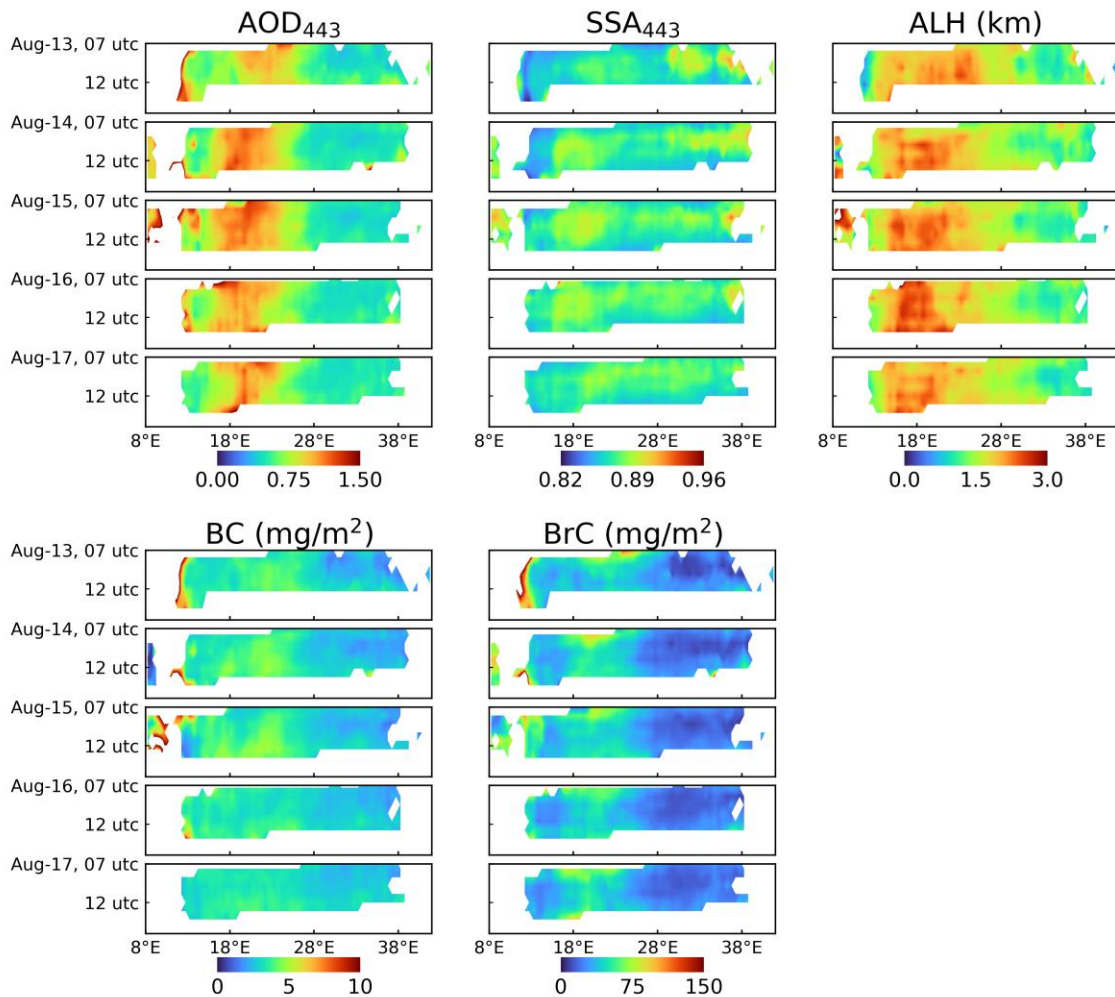
448 (Eck et al., 2013). And yet, particle size distributions tend to remain unchanged (Reid et al., 2005b;  
 449 Sayer et al., 2014). This makes the region an ideal test environment for absorption retrievals. We  
 450 selected four cases (June 8, July 26, August 14, and September 19, 2018) to illustrate the seasonal  
 451 changes in smoke regions from northeast to southwest; these align closely with the climatological  
 452 patterns detected by other ground-based and satellite measurements (Eck et al., 2013; Duncan et  
 453 al., 2003). The detected fires were subcontinent-wide (Fig 6) and generated smoke with AOD  
 454 reaching up to  $\sim 2$ . The general particle properties were consistent across the four cases. The light  
 455 absorption, reaching as low as  $\sim 0.84$   $SSA_{443}$ , was notably stronger than in the cases over North  
 456 America. The ALH of pixels with high AOD remained relatively constant at 2-3 km. High BC  
 457 concentrations (e.g.,  $> 5$   $mg/m^2$ ) were prevalent over detected fire locations despite relatively  
 458 lower AOD condition (e.g.,  $AOD_{443} < 2$ ) than in the cases over North America, where similar BC  
 459 concentrations were observed from the pixels with  $AOD_{443} > \sim 3$ .  
 460



461  
 462 Figure 6. Illustration of smoke optical properties ( $AOD_{443}$ ,  $SSA_{443}$ , ALH, and BC and BrC mass  
 463 concentrations) over Central Africa on June 8, July 26, August 14, and September 19, 2018.  
 464

465 The measurements taken over five consecutive days from August 13-17 over the Central  
 466 Africa study region detected weaker zonal smoke plume transport with less dynamic changes in  
 467 particle properties (Fig 7) compared to the North America cases (Fig 5). The relatively low ALH

468 of 2-3 km indicates that smoke aerosol mostly concentrated within the boundary layer and was  
 469 less influenced by strong jets at higher altitudes. AOD was slightly enhanced during early morning  
 470 and late afternoon by ~10-20% over 20-25°E region. The afternoon pattern is consistent with long-  
 471 term AERONET measurements shown in Eck et al. (2003), whereas the morning pattern should  
 472 be further analyzed. From SEVIRI measurements, the peak of active fires is most frequently  
 473 detected around noon (Wooster et al., 2021). Eck et al. (2003) concluded that elevated air  
 474 temperatures, reduced relative humidity, and heightened wind speeds during the midday and  
 475 afternoon periods often lead to more intense and rapidly spreading fires.



476  
 477 Figure 7. Same with Fig 5 except for over Central Africa (8-42°E, 17°S-5°N, 0.5° longitudinal  
 478 interval) from 13 to 17 August 2018.

479  
 480 The observed difference between the two regions clearly correlates with the different fuel  
 481 types – forests in North America and savannah grasses and bushes in Central Africa. For instance,

482 forest wildfires in North America with much higher thermal energy density result in elevated ALH,  
483 incomplete combustion, and higher BrC concentrations, whereas fast-spreading grassland fires are  
484 known for high BC concentration from flaming combustion emissions, but lower energy density,  
485 which keep generated smoke generally within the boundary layer over Central Africa.

486 High fuel consumption can explain higher ALH from North America with more thermal  
487 energy. Fuel consumption is defined as the amount of biomass, coarse and fine litter, and soil  
488 organic matter consumed per unit area burned. It is the product of fuel load and combustion  
489 completeness, leading to regional differences. For instance, western US, Canada, and Siberia  
490 regions categorized as boreal forests exhibit high fuel consumption (e.g.,  $> 2 \text{ kg C m}^{-2}$  burned),  
491 whereas the savanna region in Central Africa has lower fuel consumption (e.g.,  $1\text{--}2 \text{ kg C m}^{-2}$   
492 burned; van der Werf et al., 2017). The energy released along the flame front is directly related to  
493 plume height, with plumes from these fires reaching altitudes between 2.2 km and 13 km (Lavoué  
494 et al., 2000). Satellite-derived fire radiative power also shows significant differences between  
495 smoke plumes in the free troposphere (1620–1640 MW) and those within the boundary layer  
496 (174–465 MW; van der Werf et al., 2010).

### 497 **3.2 Comparison of smoke properties derived from AERONET and CALIOP**

498 The regional validation of AOD, spectral SSA, and ALH throughout 2018 using the  
499 AERONET and CALIOP datasets is presented in Fig 8. The AOD comparison over North America  
500 demonstrates a correlation coefficient ( $R$ ) of 0.91 and a root mean squared error ( $rmse$ ) of 0.22. It  
501 is important to note that this comparison only covers smoke retrievals; it excludes low AOD  
502 conditions (e.g., background AOD at 443 nm  $< 0.4$ ), that may result in lower validation statistics  
503 compared to the previous analysis incorporating the combined “background+smoke” AOD ( $R$  of  
504 0.85 and  $rmse$  of 0.13 in Lyapustin et al., 2021b). Nonetheless, the mean bias error ( $MBE$ ) of 0.02  
505 in version 3 is smaller than the 0.05 reported by Lyapustin et al. (2021b) based on v2. 74.9% of  
506 results fall within the expected error envelope for AOD, defined as  $\pm(0.05+0.2\times\text{AERONET AOD})$   
507 from AERONET AOD. Hereafter, “ $EE$ ” refers to a percentage of retrievals within the expected  
508 error envelope. Central Africa AOD also exhibits similar validation statistics, except for a lower  
509  $R$  (0.60), likely due to a narrow range of collocated AOD compared to North America. However,  
510 the  $MBE$  of  $-0.04$  and  $EE$  of 74.8% are comparable to the statistics for North America. Despite  
511 the absence of IR channels for cloud detection and the relatively coarse spatial resolution ( $>10 \text{ km}$ )  
512 of EPIC, which can lead to sub-pixel cloud contamination (Marshak et al., 2018), the achieved  
513 accuracy in AOD retrieval is very encouraging.

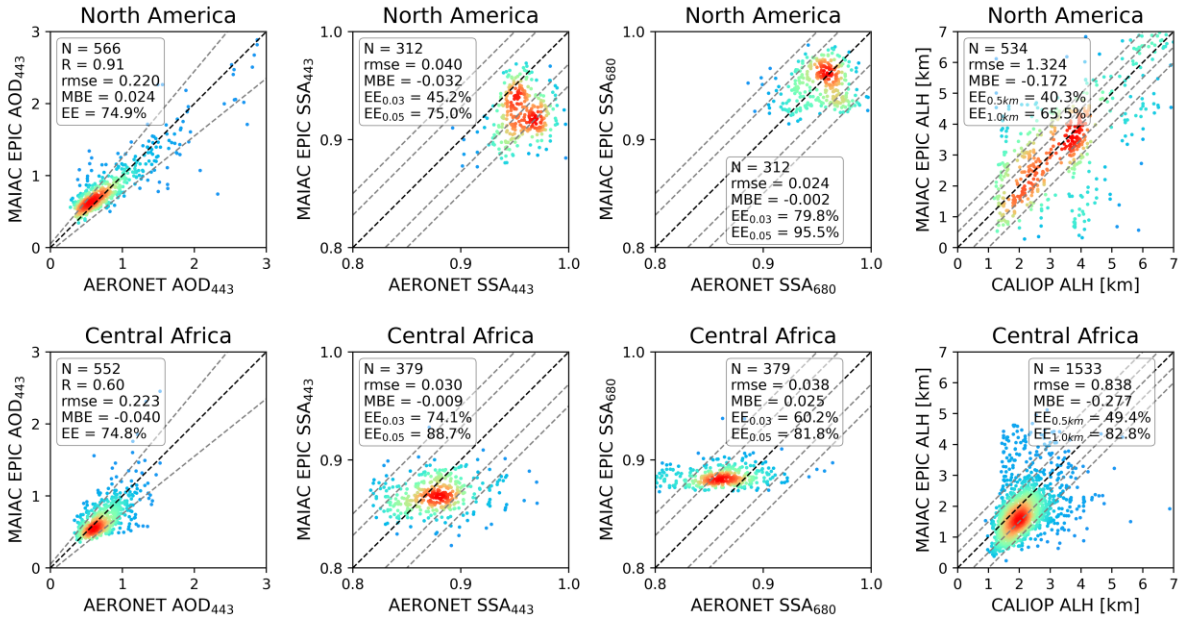
514 Regional comparisons of SSA with AERONET retrievals are more distinct than those of  
515 AOD. Overall, the  $SSA_{443}$  over North America from EPIC is lower than that from AERONET with  
516  $MBE$  of  $-0.03$  and  $EE_{0.03}$  for SSA, defined as a percentage of retrievals within  $\pm 0.03$  from  
517 AERONET SSA, is 45.2%. The collocated range spans about 0.88 to 0.97 from EPIC and 0.90-  
518 1.00 from AERONET. Comparisons over Central Africa show a much smaller bias ( $MBE$  of  $-0.01$ )  
519 and higher  $EE_{0.03}$  of 74.1%. The regional difference in accuracy could be attributed to uncertainty  
520 in our assumptions of regional smoke model properties (e.g., particle size and real refractive index).

521 Nonetheless, the retrieved MAIAC EPIC SSA<sub>443</sub> remains comparable to OMAERUV SSA<sub>440</sub>  
522 retrievals (*rmse* of 0.04 and *EE*<sub>0.03</sub> of 57.5% over North America; *rmse* of 0.04 and *EE*<sub>0.03</sub> of 66.4%  
523 over South America and Southern Africa in Jethva et al., 2014) and TropOMAER SSA<sub>440</sub> retrievals  
524 (*rmse* of 0.04 to 0.04; *EE*<sub>0.03</sub> of 48 to 51% in Torres et al., 2020). Additionally, it is worth noting  
525 that the current AERONET algorithm has a strong spectral smoothness constraint for the imaginary  
526 part of refractive indices, resulting in less representation of BrC (Sinyuk et al., 2022; Eck et al.,  
527 2023). By employing the relaxed constraint, they found decreased SSA (e.g., more absorbing) with  
528 smaller sky radiance error from wildfire cases containing a large amount of BrC. However for the  
529 biomass burning cases shown in Sinyuk et al. (2022) for both North America wildfire smoke and  
530 savanna burning smoke in Zambia the difference in spectral SSA at 443 nm were ~0.01 or less for  
531 the relaxed versus standard V3 constraints, while some differences in SSA at 675 nm were ~0.02  
532 for North American smoke only. With this update from the AERONET side, we anticipate a  
533 potentially better agreement between EPIC and AERONET for SSA<sub>443</sub> and possibly better for  
534 SSA<sub>680</sub> in the future.

535 SSA<sub>680</sub> retrievals from North America show better agreement with AERONET than SSA<sub>443</sub>  
536 with a smaller *MBE* of -0.002, *rmse* of 0.02, and higher *EE*<sub>0.03</sub> (79.8%). However, Central Africa  
537 shows slightly less agreement in SSA<sub>680</sub> compared to SSA<sub>443</sub>, with a higher positive bias (*MBE* of  
538 0.03) and smaller *EE*<sub>0.03</sub> of 60.2%. Additionally, the retrieved range of SSA<sub>680</sub> is relatively  
539 narrower (~0.87 to 0.92) than that of AERONET (~0.80 to 0.99). Regardless, the statistics metrics  
540 are much closer to POLDER GRASP SSA<sub>680</sub> retrievals (*rmse* of 0.06; *MBE* of -0.04 to -0.02 in  
541 Chen et al., 2020).

542 The comparison of EPIC ALH with CALIOP also reveals strong regional dependence.  
543 Most collocated ALH retrievals are relatively high over North America (3-4 km) and sometimes  
544 reach 6-7 km. In Central Africa, ALH ranges from 0 to 4-5 km, with most collocated retrievals  
545 falling within 1-3 km. The *rmse* value is closely related to the range of ALH; thus, it is relatively  
546 high in North America (1.32 km). More favorable validation statistics were extracted from Central  
547 Africa (*rmse* of 0.84 km; *EE*<sub>0.5km</sub> of 49.4%; *MBE* of -0.28 km), where *EE*<sub>0.5km</sub> is a percentage of  
548 retrievals within a range of ± 0.5 km from CALIOP ALH. This level of accuracy, derived from  
549 long-term validation rather than selected individual cases, is better than the operational TROPOMI  
550 ALH (*MBE* of -2.41 to -1.03 km and *rmse* of 1.97-3.56 km in Nanda et al., 2020).

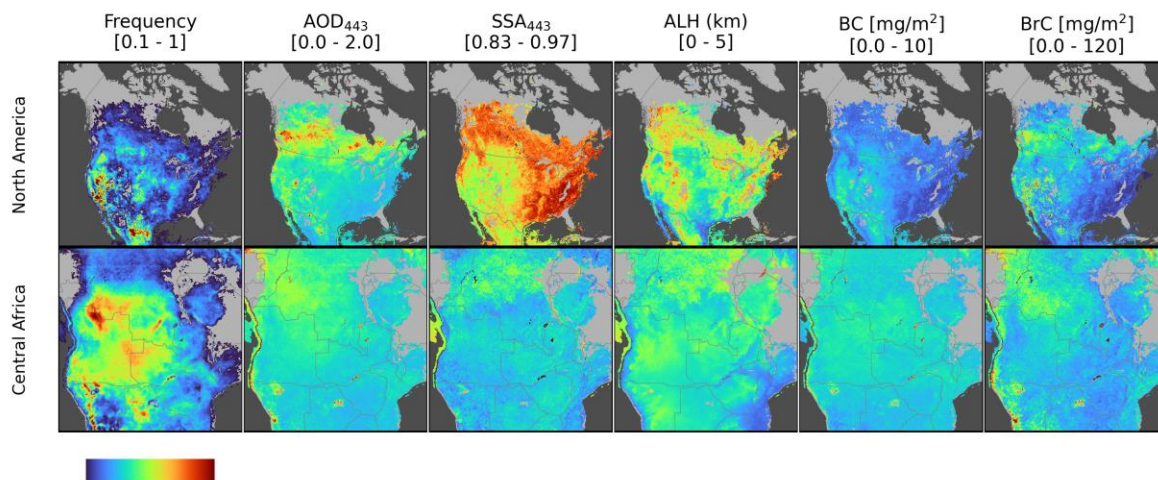
551



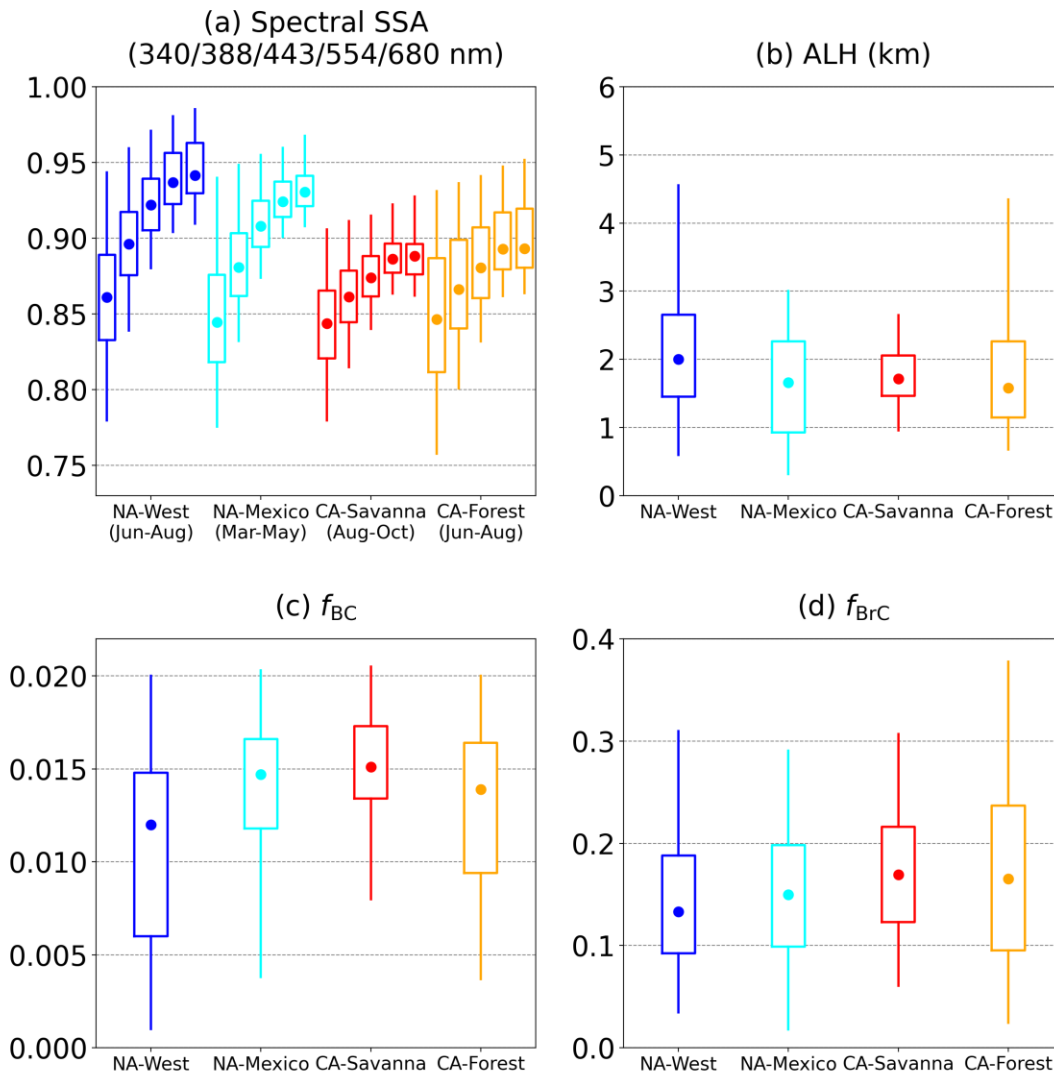
552  
 553 Figure 8. Comparison of MAIAC EPIC smoke AOD<sub>443</sub> (first column), SSA<sub>443</sub> (second column),  
 554 SSA<sub>680</sub> (third column) with AERONET, and ALH with CALIOP (fourth column). Color represents  
 555 the relative frequency of retrievals. The black dashed lines are 1:1 reference line. The gray dashed  
 556 lines are ranges of expected error envelopes:  $\pm (0.05 + 0.2 \times \text{AERONET AOD})$  from AERONET  
 557 AOD;  $\pm 0.03$  or  $\pm 0.05$  from AERONET SSA; and  $\pm 0.5$  km or  $\pm 1.0$  km from CALIOP ALH.

### 558 3.3 Regional climatology of smoke properties

559 We compiled all the smoke properties retrieved for 2018 and conducted a regional analysis  
 560 to understand their climatology and relationships with environmental factors such as vegetation  
 561 and fuel type, as well as meteorological conditions. Regional geographical distributions are  
 562 illustrated in Fig 9, and the corresponding statistical distributions are presented as box-whisker  
 563 plots in Fig 10.  
 564



565  
 566 Figure 9. Spatial distribution of relative retrieval frequency (i.e., relative number of retrievals) and  
 567 smoke properties (AOD<sub>443</sub>, SSA<sub>443</sub>, ALH, and BC and BrC mass concentrations) for 2018 over  
 568 North America (top panels) and Central Africa (bottom panels). Pixels with retrieval frequencies  
 569 lower than 10% compared to the regional maximum are filtered out. The color bar scale is indicated  
 570 at the top of each panel.



571  
 572 Figure 10. Distribution of (a) spectral SSA, (b) ALH, (c) BC volume fraction, and (d) BrC volume  
 573 fraction over western North America (“NA-West”) and Mexico (“NA-Mexico”) in North America,  
 574 and savanna (“CA-Savanna”) and tropical forest (“CA-Forest”) in Central Africa. Whiskers give  
 575 the 5<sup>th</sup> and 95<sup>th</sup> percentiles; boxes represent the 25 and 75<sup>th</sup> percentiles; and dots denote the 50<sup>th</sup>  
 576 percentile. In (a), five consecutive box-whisker plots for each region represent different  
 577 wavelengths (340, 388, 443, 554, and 680 nm from left to right).

578  
 579

580 Active wildfires occur in late spring and summer over western North America, with  
 581 expanded burned areas over the years (Dennison et al., 2014; Kalashnikova et al., 2018; Liu et al.,  
 582 2010). Most smoke retrievals were detected over the western United States (e.g., California,

583 Oregon, Washington) and western Canada (e.g., British Columbia) (Fig 9). The optical properties  
584 were quite distinct between source regions and downwind regions. The western US and western  
585 Canada source regions show relatively low SSA and ALH, while central Canada, which is a source  
586 region, but also mostly downwind regions for transported heavy smoke plume from western  
587 regions, show higher SSA and ALH. This difference is closely related to the smoke aging process  
588 discussed in Sec 3.1.1. Spatiotemporally integrated spectral SSA over western North America  
589 (“NA-West” region in Fig 2) of 0.86, 0.89, 0.92, 0.94, and 0.95 at 340, 388, 443, 554, and 680 nm,  
590 respectively, align with the range 0.915-0.935 at 443 nm and 0.95-0.97 at 680 nm derived from  
591 multiple AREONET measurements in September 2020 (Eck et al., 2023). The mean and standard  
592 deviation of ALH was  $2.2 \pm 1.2$  km with a wide range of values up to 4.6 km at the 95th percentile  
593 (Fig 10b). The mean BC volume fraction of  $0.011 \pm 0.006$  was the lowest among the selected  
594 regions. The number of smoke pixels was maximum in August, with the highest BrC mass  
595 concentration (median value of  $29 \text{ mg/m}^2$ ), synchronized with seasonal wildfire activities over  
596 western North America. Although BC and BrC concentrations can reach up to more than  $5 \text{ mg/m}^2$   
597 and  $100 \text{ mg/m}^2$ , respectively, over some specific regions (Fig 9), the averaged values were not as  
598 high due to high spatiotemporal variation. Another smoke-dominated region in North America is  
599 found over Mexico (“NA-Mexico” region in Fig 2), where both natural wildfires and agricultural  
600 burns occur annually during the hot and dry season (March to May; Rios et al., 2023). This region  
601 exhibited smoke properties with more absorption and lower ALH with lower variation ( $1.6 \pm 0.9$   
602 km) than western US.

603 Central Africa is climatologically the largest global biomass burning source, peaking  
604 during the austral winter. The region contributes approximately one-third of Earth’s biomass  
605 burning emissions from various sources, including wildfires, agricultural fires, and industrial  
606 activities (van der Werf et al., 2010). The distribution of smoke retrievals appears relatively  
607 homogeneous and similar to that of detected fires, with widespread retrieval frequency in Angola,  
608 Democratic Republic of the Congo, and Zambia, and more varied sources in Namibia (Fig 9).  
609 During the August–October burning season in Central Africa, aerosol light-absorption is  
610 predominantly attributed to BC, a byproduct of savanna burning characterized by significant  
611 flaming-phase combustion (Ward et al., 1996). Although the retrieved smoke AOD is not as high  
612 as in North America, light absorption over savanna region in Central Africa (“CA-Savanna” region  
613 in Fig 2) was more substantial, leading to higher BC and BrC mass concentrations. Low SSA  
614 spanned from UV through the visible (0.84, 0.86, 0.88, 0.89, and 0.89 at 340, 388, 443, 554, and  
615 680 nm, respectively), with higher BC and BrC volume fractions of 0.015 and 0.178, respectively.  
616 The ALH is lower and less variance ( $1.8 \pm 0.6$  km; 2.6 km for the 95<sup>th</sup> percentile) that of western  
617 North America. The BC and BrC mass concentrations increased from July, peaked in September  
618 (median values of  $3.3 \text{ mg/m}^2$  and  $28.4 \text{ mg/m}^2$ , respectively), and declined toward November; this  
619 aligns with long-term AERONET AOD measurements (Eck et al., 2003) and with AERONET-  
620 based BC and BrC estimations (Schuster et al., 2016). By contrast, smoke from tropical forest fires  
621 in Central Africa (“CA-Forest” region in Fig 2) shows slightly less absorption with lower BC  
622 volume fraction (0.013) and larger variabilities of BrC volume fraction ( $0.018 \pm 0.11$ ) and ALH



623 (1.9 ± 1.1 km) than that of savanna region. BC and BrC mass concentrations over the tropical  
624 forest region in Central Africa peak in July (earlier than savanna region) with lower BC (2.8 mg/m<sup>2</sup>)  
625 and higher BrC (37.8 mg/m<sup>2</sup>) than those of the savanna region.

## 626 4. Discussions

### 627 4.1 Comparison of the BrC to BC mass concentration ratio with other studies

628 The ratio between OC and EC (OC/EC) is widely used to elucidate the apportionment of  
629 carbonaceous components in smoke particles as a proxy for assessing the dominance of primary  
630 emissions from flaming combustion (e.g., fossil fuel) versus smoldering combustion emissions  
631 and secondary formation of OC (e.g., biomass burning, wildfires, secondary organic aerosol (SOA)  
632 formation) (Lim and Turpin, 2002; Pokhrel et al., 2016). As BrC is an absorbing OC among total  
633 OC, we inferred regional BrC-to-BC column mass concentration ratios (BrC/BC) from EPIC and  
634 compared them with those from other studies providing BrC/BC or OC/EC.

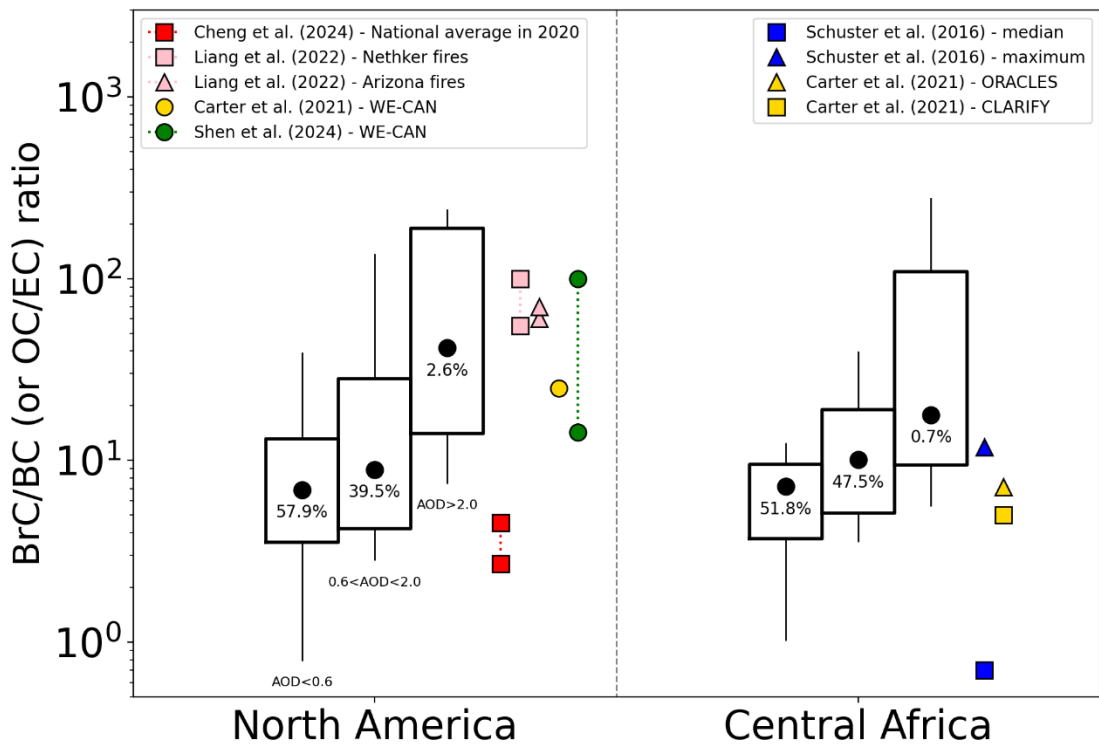
635 Results of BrC/BC ratio from this study in North America and Central Africa are compared  
636 with other previous studies in Fig 11. The absolute BC and BrC volume fractions in Central Africa  
637 were higher than in North America, resulting in similar median values of the BrC/BC mass  
638 concentration ratio (7.3 for North America and 8.0 for Central Africa). When the ratios are  
639 categorized into different AOD ranges, the BrC/BC increases with AOD from both regions. For  
640 two groups of AOD < 0.6 (“low-moderate AOD”) and 0.6 < AOD < 2.0 (“high AOD”), the median  
641 BrC/BC is higher in Central Africa (7.2 and 10.1) than in North America (6.9 and 8.9). The  
642 variance, represented as the range of estimations, is more significant in North America for the two  
643 groups, which could be ascribed to more diverse fuel types from natural, residential, and  
644 agricultural sources and related emission processes (Xiong et al., 2022). For the cases of AOD >  
645 2.0 (“extremely high AOD”), which corresponds to 2.6% and 0.7% of the entire retrieval record  
646 in North America and Central Africa, respectively, North America showed a higher BrC/BC ratio  
647 (median value of 41.5) with a higher variance than Central Africa (median value of 17.7). This  
648 higher BrC/BC ratio in North America, compared to Central Africa, may have its origin in more  
649 common smoldering combustion and/or more SOA formation during transport. Most “extremely  
650 high AOD” cases were observed from transport plumes, where the increased BrC/BC ratio is  
651 associated with their aging processes including SOA formation. These results are consistent with  
652 POLDER/GRASP and MISR aerosol components analysis (Li et al., 2022; Junghenn Noyes et al.,  
653 2022).

654 Our estimates exhibit relatively high variance because they encompassed all pixels detected  
655 as smoke in the retrieval algorithm over the continents in 2018, rather than being limited to selected  
656 heavy plumes. The national average of OC/EC ratio (3.6±0.9) obtained from U.S. EPA ground-  
657 based chemical composition measurement networks (including CSN and IMPROVE) for all  
658 sources, not only for smoke sources, (Cheng et al., 2024) falls within the estimates from EPIC’s  
659 “low-moderate AOD” group. OC/EC ratios obtained from specific wildfire samples including WE-  
660 CAN campaign during 2018 July-September over western US (Liang et al., 2022; Carter et al.,

2021) range from approximately 14 to 100, corresponding to the “extremely high AOD” group. It is important to note that although the BrC/BC ratio is smaller than the OC/EC ratio, obtaining an accurate BrC/BC is challenging without proper measurements separating BrC from OC, which is rarely done in experiments.

The ORACLES (August–September 2016) and CLARIFY (August 2017) campaigns over the eastern South Atlantic Ocean (Carter et al., 2021) measured transported smoke aerosols from Central Africa. The general level of AOD at 550 nm for both campaigns was ~0.3 to ~0.7 (Haywood et al., 2021; Sayer et al., 2019), and corresponding OC/EC ratios were 5-7, which are consistent with the estimated EPIC ranges for “low-moderate AOD” and “high AOD”. Another comparison can be made with the BrC/BC mass concentration ratio inferred from AERONET measurements (Schuster et al., 2016). Although the definition is similar to ours, both using column-integrated and remote-sensing-based values, it shows relatively lower values than ours. This difference could be attributable to the different wavelengths (i.e., UV-Vis for EPIC, Vis-NIR for AERONET) used for the measurements and different assumptions in the components (e.g., dependence of composition on particle size in Schuster et al., 2016).

The EPIC BrC/BC ratios increased with AOD, representing aging processes during transport over North America and Central Africa. They are generally consistent with other studies despite different measurement characteristics, such as OC/EC vs. BrC/BC, and *in-situ* versus remote sensing.



680

681 Fig 11. Regional EPIC-derived BrC to BC column mass concentration ratios across three AOD  
682 ranges ( $AOD < 0.6$ ,  $0.6 < AOD < 2.0$ , and  $AOD > 2.0$ ). Each box-whisker plot comprises the 5<sup>th</sup>,  
683 15.9<sup>th</sup>, 50<sup>th</sup>, 84.1<sup>st</sup>, and 95<sup>th</sup> percentiles. The percentages of retrievals per each AOD range are  
684 denoted within the box. On the right side of each region panel, the values (or range) of the BrC-  
685 to-BC ratio (only for Schuster et al., 2016) or OC-to-BC ratio (all others) from other studies are  
686 shown.

#### 687 **4.2 Uncertainty of volume fractions due to assumed BC and BrC refractive indices**

688 Assumed spectral imaginary refractive indices of BC and BrC determine their inferred  
689 volume fractions. Identical spectral absorption can result in lower BC and BrC fractions with  
690 higher BC and BrC imaginary refractive indices and vice versa. As most satellite measurements,  
691 including EPIC, lack sensitivity to infer both the imaginary refractive indices of inclusions and  
692 their volume fractions, we must assume the imaginary refractive indices of inclusions to infer their  
693 volume fractions. Here, we investigate the effect of this assumption on the inferred volume  
694 fractions and assess the resulting uncertainties.

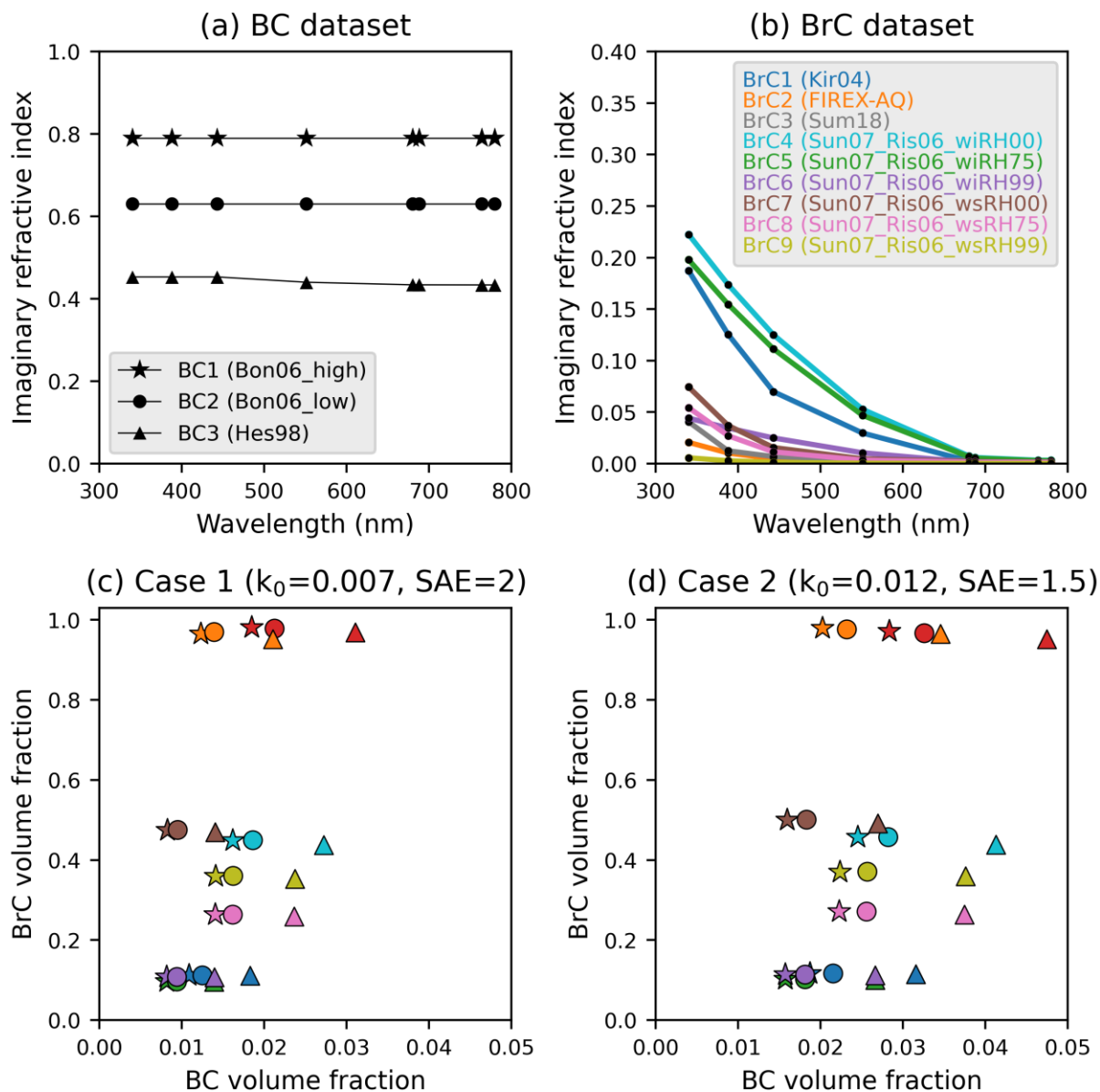
695 A total of three different BC datasets were considered (Fig 12a). “BC1”, which we used,  
696 and “BC2” were derived from multiple measurements combined with the assumption that light-  
697 absorbing carbon has a single refractive index and that variation can be expressed by the  
698 Bruggeman effective-medium theory (Bond and Bergstrom, 2006). “BC3”, utilized in aerosol  
699 modeling for AirMSPI analysis (Kalashnikova et al., 2018), was originally referred to as the “soot”  
700 component of the Optical Properties of Aerosols and Clouds (OPAC) dataset described in Hess et  
701 al. (1998). The value of  $k$  is between 0.4 and 0.8 and is spectrally invariant or nearly invariant.

702 We tested nine different BrC datasets (Fig 12b). “BrC1”, which we used, was derived from  
703 organic carbon extracted from wood burning and SAFARI biomass smoke samples as described  
704 in Kirchstetter et al. (2004). “BrC2” is an Air-MSPI retrieved value during the FIREX-AQ  
705 campaign (O. Kalashnikova, personal communication, May 19, 2020). “BrC3” represents aerosols  
706 emitted from the smoldering combustion of Boreal and Indonesian peatlands (Sumlin et al., 2018).  
707 “BrC4”, “BrC5”, and “BrC6” represent water-insoluble BrC with relative humidity of 0%, 75%,  
708 and 99%, respectively, calculated by combining the upper curve of Sun et al. (2007) and  
709 hygroscopic properties in Rissler et al. (2006). “BrC7”, “BrC8”, and “BrC9” are the same but  
710 represent water-soluble BrC. These datasets were obtained from the Table of Aerosol Optics (TAO)  
711 dataset within the framework of the Models, In situ, and Remote sensing of Aerosols (MIRA)  
712 working group projects (<https://science.larc.nasa.gov/mira-wg/>).

713 Here, two smoke cases were analyzed: “Case 1” ( $k_0$  of 0.007 and SAE of 2) and “Case 2”  
714 ( $k_0$  of 0.012 and SAE of 1.5), representing the most populated EPIC retrievals in the AERONET  
715 validation over North America and Central Africa, respectively. For Case 1, the  $f_{BC}$  and  $f_{BrC}$  based  
716 on our current assumptions are 0.011 and 0.112, respectively (marked with a “star” marker in dark  
717 blue in Fig 12c). With different assumptions for inclusion properties, they have a range of 0.008-  
718 0.031 and 0.096-0.982, respectively. Less absorbing BC assumptions (i.e., smaller  $k$ ) result in  
719 increased  $f_{BC}$  to 0.012 (“BC2” and “BrC1”) and 0.018 (“BC3” and “BrC2”). The maximum

720 difference of  $f_{\text{BC}}$  is 0.013, with the lowest absorption in BrC (“BrC9”). The potential  $f_{\text{BrC}}$  values  
721 exhibit greater variability. The  $f_{\text{BrC}}$  value with the current assumption (0.112) is one of the lowest  
722 values among tested combinations and similar to those from “BrC2” and “BrC3”, which have  
723 stronger absorption than others. The BrC assumptions with less absorbing properties show higher  
724  $f_{\text{BrC}}$  from 0.264 to 0.981. We also tested the spectral  $k$  for dark BrC obtained from the FIREX-AQ  
725 campaign in the western US (Chakrabarty et al., 2023). They showed an estimated  $f_{\text{BC}}$  close to  
726 zero because of the relatively high  $k$  of 0.1 at 680 nm. Case 2 is converted to higher  $f_{\text{BC}}$  (0.019)  
727 and similar  $f_{\text{BrC}}$  (0.117) compared to Case 1 with the default assumption. The range of  $f_{\text{BC}}$  and  
728  $f_{\text{BrC}}$  from the different combinations is 0.016-0.047 and 0.101-0.980, respectively. It is essential  
729 to acknowledge that inferring volume fractions and mass concentrations is based on assumed  
730 inclusion properties, introducing some uncertainties. The assumed properties of BC and BrC will  
731 need to be refined in future studies (e.g., a suggested concept in Kahn et al., 2017) to enhance the  
732 accuracy of our findings.

733



734  
 735 Fig 12. Spectral imaginary refractive indices of (a) BC and (b) BrC. Range of BC and BrC volume  
 736 fractions for (c) “Case 1” ( $k_0$  of 0.007 and  $SAE$  of 2) and (d) “Case 2” ( $k_0$  of 0.012 and  $SAE$  of  
 737 1.5). The star, circle, and triangle symbols in (c) and (d) refer to different BC assumptions of  
 738 “BC1”, “BC2”, and “BC3” in (a). The different colors in (c) and (d) refer to different BrC  
 739 assumptions from “BrC1” to “BrC9” in (b).

740

741 **5. Summary and conclusions**

742 This study introduced a technique inferring the BC and BrC light-absorbing components  
 743 of smoke aerosol by leveraging the spectral absorption retrieved in the MAIAC EPIC algorithm.

744 Spectral absorption retrievals allowed us to quantify the BC and BrC fractions, which were then  
745 converted to column-integrated mass concentrations assuming the particle mass extinction  
746 efficiency. We assumed that BC and BrC are internally mixed with a non-absorbing host  
747 representing non-absorbing OC, sulfate, nitrate, or ammonium components, using the Maxwell  
748 Garnett effective medium approximation.

749 We analyzed regional characteristics over North America and Central Africa in 2018,  
750 utilizing all available MAIAC EPIC smoke property retrievals (AOD, spectral SSA, ALH, and BC  
751 and BrC volume fractions and mass concentrations). Selected cases showed that smoke aerosols  
752 emitted from wildfires over western North America exhibited extremely high AOD up to ~6 with  
753 elevated ALH (6-7 km). Dynamic changes in spectral absorption and significant BrC components  
754 were observed during continental-scale transport. The MAIAC EPIC products successfully  
755 monitored the transport and evolution of smoke optical properties with high temporal resolution  
756 during regional-to-continental-scale transport. Biomass-burning smoke over Central Africa  
757 displayed higher absorption with greater BC and BrC fractions than North America, showing  
758 seasonal changes in major source locations. They also showed less strong zonal transport with  
759 ALH closer to the surface, and diurnal change in smoke amounts related to fire activities.

760 EPIC-retrieved AOD<sub>443</sub>, SSA<sub>443</sub>, SSA<sub>680</sub>, and ALH agreed with collocated AERONET and  
761 CALIOP measurements with *rmse* of 0.2, 0.03-0.04, 0.02-0.04, and 0.8-1.3 km, respectively, and  
762 the overall accuracies were comparable to other operational satellite products such as OMI,  
763 TROPOMI, and POLDER. Spatiotemporally integration of measurements revealed geographical  
764 characteristics and distinct differences in optical properties, ALH, and inferred BC and BrC,  
765 closely linked to burning types and meteorological conditions. Smoke from forest fires in western  
766 North America shows SSA<sub>443</sub> of 0.92 with low BC volume fraction of 0.011 and high ALH with  
767 larger standard deviation ( $2.2 \pm 1.2$  km). The wildfires and agricultural fires over the Mexico  
768 region generated smoke with more absorption and lower ALH. The Savanna region in Central  
769 Africa during August to October shows smoke properties with most absorbing with high BC and  
770 BrC volume fractions (0.015 and 0.178, respectively) and lower ALH with smaller variation.  
771 Smoke from tropical forests in Central Africa exhibits absorption between that of western US and  
772 savanna regions and high ALH variability. The impact of assumed imaginary refractive indices of  
773 BC and BrC in estimating their volume fractions was analyzed based on a literature survey,  
774 presenting the corresponding uncertainty ranges of our retrievals.

775 Although we focused on North America and Central Africa, smoke aerosols have a  
776 significant impact on air quality and climate globally. Future studies will extend the analysis to  
777 other regions using almost a decade of EPIC measurements since 2015, with extensive validation  
778 and error analysis using multiple measurements, including AERONET, CALIOP, and in-situ  
779 aerosol composition data.

780 The MAIAC EPIC smoke aerosol components presented here could serve as valuable *a*  
781 *priori* information for recent and upcoming satellite missions such as the Plankton, Aerosol, Cloud,  
782 ocean Ecosystem (PACE; <https://pace.gsfc.nasa.gov/>) (Remer et al., 2019a, b), the Multi-Angle  
783 Imager for Aerosols (MAIA; <https://maia.jpl.nasa.gov/>) (Diner et al., 2018), EPS-SG Multi-

784 Viewing Multi-Channel Multi-Polarisation Imaging (3MI) (Fougnie et al., 2018) and Atmosphere  
785 Observing System (AOS; <https://aos.gsfc.nasa.gov/>), focusing on retrieving aerosol microphysical  
786 and optical properties, and inferring chemical composition, with higher accuracy from multi-angle  
787 polarization measurements. Integration of our results with other in-situ and remote sensing  
788 measurements and models (e.g., Kahn et al., 2023) should enhance our understanding of smoke  
789 aerosol aging processes, improve air quality monitoring and forecasting, and refine the  
790 quantification of radiative forcing due to smoke aerosols on a global scale.

## 791 **Author contributions**

792 M. Choi and AL designed the study with discussions with GLS and SG. GLS provided  
793 major guidance on developing the BC and BrC estimation algorithms. AL and WY provided the  
794 MAIAC EPIC products. AL and SK conducted RT calculations (LUTs for MAIAC). M. Choi, AL,  
795 YW and SG developed the code and performed the retrievals. GLS and OK participated in the  
796 collection of refractive indices data. M. Choi, AL, GLS, and SG analyzed the results. M. Choi and  
797 AL wrote the manuscript with comments from all co-authors.

## 798 **Competing interests**

799 The authors declare that they have no conflict of interest.

## 800 **Data availability**

801 The retrievals can be requested directly from the corresponding author  
802 (myungje.choi@nasa.gov) or Dr. Alexei Lyapustin (alexey.i.lyapustin@nasa.gov).

## 803 **Acknowledgment**

804 The work of A. Lyapustin, M. Choi, S. Go, and Y. Wang was funded by the NASA  
805 DSCOVR program (21-DSCOVR-21-0004; manager Dr. R. Eckman) and in part by the NASA  
806 PACE program (19-PACESAT19-0039). J. S Reid was funded by the Office of Naval Research,  
807 Code 322. The work of H. Moosmüller was supported in part by the National Science Foundation  
808 under Grant No. OIA- 2148788 and by NASA under grant 80NSSC20M0205 (PACE SAT Project:  
809 PACE UV ROAD). We are grateful to the AERONET team for providing validation data and to  
810 the NASA Center for Climate Simulations providing resources for the EPIC data processing.

## 811 **References**

812 Ahn, C., Torres, O., Jethva, H., Tiruchirapalli, R., and Huang, L.-K.: Evaluation of Aerosol  
813 Properties Observed by DSCOVR/EPIC Instrument From the Earth-Sun Lagrange 1 Orbit, J.  
814 Geophys. Res. Atmos., 126, e2020JD033651,

815 <https://doi.org/https://doi.org/10.1029/2020JD033651>, 2021.

816 Andreae, M. O.: Emission of trace gases and aerosols from biomass burning – an updated  
817 assessment, *Atmos. Chem. Phys.*, 19, 8523–8546, <https://doi.org/10.5194/acp-19-8523-2019>,  
818 2019.

819 Andreae, M. O. and Gelencsér, A.: Black carbon or brown carbon? the nature of light-absorbing  
820 carbonaceous aerosols, *Atmos. Chem. Phys.*, 6, 3131–3148, <https://doi.org/10.5194/acp-6-3131-2006>, 2006.

822 Andreae, M. O. and Merlet, P.: Emission of trace gases and aerosols from biomass burning, *Global  
823 Biogeochem. Cycles*, 15, 955–966, <https://doi.org/10.1029/2000GB001382>, 2001.

824 Bellouin, N., Boucher, O., Haywood, J., and Reddy, M. S.: Global estimate of aerosol direct  
825 radiative forcing from satellite measurements, *Nature*, 438, 1138–1141,  
826 <https://doi.org/10.1038/nature04348>, 2005.

827 Bhandari, J., China, S., Chandrakar, K. K., Kinney, G., Cantrell, W., Shaw, R. A., Mazzoleni, L.  
828 R., Giroto, G., Sharma, N., Gorkowski, K., Gilardoni, S., Decesari, S., Facchini, M. C., Zanca,  
829 N., Pavese, G., Esposito, F., Dubey, M. K., Aiken, A. C., Chakrabarty, R. K., Moosmüller,  
830 H., Onasch, T. B., Zaveri, R. A., Scarnato, B. V., Fialho, P., and Mazzoleni, C.: Extensive  
831 Soot Compaction by Cloud Processing from Laboratory and Field Observations, *Sci. Rep.*, 9,  
832 <https://doi.org/10.1038/s41598-019-48143-y>, 2019.

833 Bohren, C. F. and Huffman, D. R.: *Absorption and Scattering of Light by Small Particles*, Wiley,  
834 <https://doi.org/10.1002/9783527618156>, 1998.

835 Bond, T. C. and Bergstrom, R. W.: *Light Absorption by Carbonaceous Particles: An Investigative  
836 Review*, *Aerosol Sci. Technol.*, 40, 27–67, <https://doi.org/10.1080/02786820500421521>,  
837 2006.

838 Bond, T. C., Doherty, S. J., Fahey, D. W., Forster, P. M., Berntsen, T., Deangelo, B. J., Flanner,  
839 M. G., Ghan, S., Kärcher, B., Koch, D., Kinne, S., Kondo, Y., Quinn, P. K., Sarofim, M. C.,  
840 Schultz, M. G., Schulz, M., Venkataraman, C., Zhang, H., Zhang, S., Bellouin, N., Guttikunda,  
841 S. K., Hopke, P. K., Jacobson, M. Z., Kaiser, J. W., Klimont, Z., Lohmann, U., Schwarz, J.  
842 P., Shindell, D., Storelvmo, T., Warren, S. G., and Zender, C. S.: Bounding the role of black  
843 carbon in the climate system: A scientific assessment, *J. Geophys. Res. Atmos.*, 118, 5380–  
844 5552, <https://doi.org/10.1002/jgrd.50171>, 2013.

845 Bond, W. J. and Keeley, J. E.: Fire as a global “herbivore”: the ecology and evolution of flammable  
846 ecosystems., *Trends Ecol. Evol.*, 20, 387–94, <https://doi.org/10.1016/j.tree.2005.04.025>,  
847 2005.

848 Carter, T. S., Heald, C. L., Cappa, C. D., Kroll, J. H., Campos, T. L., Coe, H., Cotterell, M. I.,  
849 Davies, N. W., Farmer, D. K., Fox, C., Garofalo, L. A., Hu, L., Langridge, J. M., Levin, E. J.  
850 T., Murphy, S. M., Pokhrel, R. P., Shen, Y., Szpek, K., Taylor, J. W., and Wu, H.:  
851 Investigating Carbonaceous Aerosol and Its Absorption Properties From Fires in the Western  
852 United States (WE-CAN) and Southern Africa (ORACLES and CLARIFY), *J. Geophys. Res.*  
853 *Atmos.*, 126, 647–650, <https://doi.org/10.1029/2021JD034984>, 2021.

854 Chakrabarty, R. K., Moosmüller, H., Chen, L.-W. A., Lewis, K., Arnott, W. P., Mazzoleni, C.,  
855 Dubey, M. K., Wold, C. E., Hao, W. M., and Kreidenweis, S. M.: Brown carbon in tar balls  
856 from smoldering biomass combustion, *Atmos. Chem. Phys.*, 10, 6363–6370,  
857 <https://doi.org/10.5194/acp-10-6363-2010>, 2010.

858 Chakrabarty, R. K., Shetty, N. J., Thind, A. S., Beeler, P., Sumlin, B. J., Zhang, C., Liu, P., Idrobo,  
859 J. C., Adachi, K., Wagner, N. L., Schwarz, J. P., Ahern, A., Sedlacek, A. J., Lambe, A., Daube,  
860 C., Lyu, M., Liu, C., Herndon, S., Onasch, T. B., and Mishra, R.: Shortwave absorption by



861 wildfire smoke dominated by dark brown carbon, *Nat. Geosci.*,  
862 <https://doi.org/10.1038/s41561-023-01237-9>, 2023.

863 Chen, C., Dubovik, O., Fuertes, D., Litvinov, P., Lapyonok, T., Lopatin, A., Ducos, F., Derimian,  
864 Y., Herman, M., Tanré, D., Remer, L. A., Lyapustin, A., Sayer, A. M., Levy, R. C., Christina  
865 Hsu, N., Descloitres, J., Li, L., Torres, B., Karol, Y., Herrera, M., Herreras, M., Aspetsberger,  
866 M., Wanzenboeck, M., Bindreiter, L., Marth, D., Hangler, A., and Federspiel, C.: Validation  
867 of GRASP algorithm product from POLDER/PARASOL data and assessment of multi-  
868 angular polarimetry potential for aerosol monitoring, *Earth Syst. Sci. Data*, 12, 3573–3620,  
869 <https://doi.org/10.5194/essd-12-3573-2020>, 2020.

870 Cheng, B., Alapaty, K., and Arunachalam, S.: Spatiotemporal trends in PM<sub>2.5</sub> chemical  
871 composition in the conterminous U.S. during 2006–2020, *Atmos. Environ.*, 316, 120188,  
872 <https://doi.org/10.1016/j.atmosenv.2023.120188>, 2024.

873 Choi, Y., Ghim, Y. S., Zhang, Y., Park, S. M., and Song, I. H.: Estimation of surface concentrations  
874 of black carbon from long-term measurements at aeronet sites over Korea, *Remote Sens.*, 12,  
875 1–24, <https://doi.org/10.3390/rs12233904>, 2020.

876 Corbin, J. C., Modini, R. L., and Gysel-Beer, M.: Mechanisms of soot-aggregate restructuring and  
877 compaction, *Aerosol Sci. Technol.*, 57, 89–111,  
878 <https://doi.org/10.1080/02786826.2022.2137385>, 2023.

879 Dennison, P. E., Brewer, S. C., Arnold, J. D., and Moritz, M. A.: Large wildfire trends in the  
880 western United States, 1984–2011, *Geophys. Res. Lett.*, 41, 2928–2933,  
881 <https://doi.org/10.1002/2014GL059576>, 2014.

882 Diner, D. J., Boland, S. W., Brauer, M., Bruegge, C., Burke, K. A., Chipman, R., Di Girolamo, L.,  
883 Garay, M. J., Hasheminassab, S., and Hyer, E.: Advances in multiangle satellite remote  
884 sensing of speciated airborne particulate matter and association with adverse health effects:  
885 from MISR to MAIA, *J. Appl. Remote Sens.*, 12, 1, <https://doi.org/10.1117/1.JRS.12.042603>,  
886 2018.

887 Dubovik, O. and King, M. D.: A flexible inversion algorithm for retrieval of aerosol optical  
888 properties from Sun and sky radiance measurements, *J. Geophys. Res. Atmos.*, 105, 20673–  
889 20696, <https://doi.org/10.1029/2000JD900282>, 2000.

890 Dubovik, O., Holben, B., Eck, T. F., Smirnov, A., Kaufman, Y. J., King, M. D., Tanré, D., and  
891 Slutsker, I.: Variability of Absorption and Optical Properties of Key Aerosol Types Observed  
892 in Worldwide Locations, *J. Atmos. Sci.*, 59, 590–608, [https://doi.org/10.1175/1520-0469\(2002\)059<0590:VOAAOP>2.0.CO;2](https://doi.org/10.1175/1520-0469(2002)059<0590:VOAAOP>2.0.CO;2), 2002.

894 Dubovik, O., Sinyuk, A., Lapyonok, T., Holben, B. N., Mishchenko, M., Yang, P., Eck, T. F.,  
895 Volten, H., Muñoz, O., Veihelmann, B., van der Zande, W. J., Leon, J. F., Sorokin, M., and  
896 Slutsker, I.: Application of spheroid models to account for aerosol particle nonsphericity in  
897 remote sensing of desert dust, *J. Geophys. Res. Atmos.*, 111, 1–34,  
898 <https://doi.org/10.1029/2005JD006619>, 2006.

899 Dubovik, O., Herman, M., Holdak, A., Lapyonok, T., Tanré, D., Deuzé, J. L., Ducos, F., Sinyuk,  
900 A., and Lopatin, A.: Statistically optimized inversion algorithm for enhanced retrieval of  
901 aerosol properties from spectral multi-angle polarimetric satellite observations, *Atmos. Meas.*  
902 *Tech.*, 4, 975–1018, <https://doi.org/10.5194/amt-4-975-2011>, 2011.

903 Dubovik, O., Lapyonok, T., Litvinov, P., Herman, M., Fuertes, D., Ducos, F., Torres, B., Derimian,  
904 Y., Huang, X., Lopatin, A., Chaikovskiy, A., Aspetsberger, M., and Federspiel, C.: GRASP:  
905 a versatile algorithm for characterizing the atmosphere, *SPIE Newsroom*,  
906 <https://doi.org/10.1117/2.1201408.005558>, 2014.

907 Duncan, B. N., Martin, R. V., Staudt, A. C., Yevich, R., and Logan, J. A.: Interannual and seasonal  
908 variability of biomass burning emissions constrained by satellite observations, *J. Geophys.*  
909 *Res. Atmos.*, 108, <https://doi.org/10.1029/2002JD002378>, 2003.

910 Eck, T. F., Holben, B. N., Reid, J. S., Dubovik, O., Smirnov, A., O’Neill, N. T., Slutsker, I., and  
911 Kinne, S.: Wavelength dependence of the optical depth of biomass burning, urban, and desert  
912 dust aerosols, *J. Geophys. Res.*, 104, 31333, <https://doi.org/10.1029/1999JD900923>, 1999.

913 Eck, T. F., Holben, B. N., Ward, D. E., Mukelabai, M. M., Dubovik, O., Smirnov, A., Schafer, J.  
914 S., Hsu, N. C., Piketh, S. J., Queface, A., Le Roux, J., Swap, R. J., and Slutsker, I.: Variability  
915 of biomass burning aerosol optical characteristics in southern Africa during the SAFARI 2000  
916 dry season campaign and a comparison of single scattering albedo estimates from radiometric  
917 measurements, *J. Geophys. Res. Atmos.*, 108, <https://doi.org/10.1029/2002jd002321>, 2003.

918 Eck, T. F., Holben, B. N., Reid, J. S., Mukelabai, M. M., Piketh, S. J., Torres, O., Jethva, H. T.,  
919 Hyer, E. J., Ward, D. E., Dubovik, O., Sinyuk, A., Schafer, J. S., Giles, D. M., Sorokin, M.,  
920 Smirnov, A., and Slutsker, I.: A seasonal trend of single scattering albedo in southern African  
921 biomass-burning particles: Implications for satellite products and estimates of emissions for  
922 the world’s largest biomass-burning source, *J. Geophys. Res. Atmos.*, 118, 6414–6432,  
923 <https://doi.org/10.1002/jgrd.50500>, 2013.

924 Eck, T. F., Holben, B. N., Reid, J. S., Sinyuk, A., Giles, D. M., Arola, A., Slutsker, I., Schafer, J.  
925 S., Sorokin, M. G., Smirnov, A., LaRosa, A. D., Kraft, J., Reid, E. A., O’Neill, N. T., Welton,  
926 E. J., and Menendez, A. R.: The extreme forest fires in California/Oregon in 2020: Aerosol  
927 optical and physical properties and comparisons of aged versus fresh smoke, *Atmos. Environ.*,  
928 305, <https://doi.org/10.1016/j.atmosenv.2023.119798>, 2023.

929 Fougnie, B., Marbach, T., Lacan, A., Lang, R., Schlüssel, P., Poli, G., Munro, R., and Couto, A.  
930 B.: The multi-viewing multi-channel multi-polarisation imager – Overview of the 3MI  
931 polarimetric mission for aerosol and cloud characterization, *J. Quant. Spectrosc. Radiat.*  
932 *Transf.*, 219, 23–32, <https://doi.org/10.1016/j.jqsrt.2018.07.008>, 2018.

933 Garnett, J. C. M.: XII. Colours in metal glasses and in metallic films, *Philos. Trans. R. Soc. London.*  
934 *Ser. A, Contain. Pap. a Math. or Phys. Character*, 203, 385–420,  
935 <https://doi.org/10.1098/rsta.1904.0024>, 1904.

936 Giles, D. M., Holben, B. N., Eck, T. F., Sinyuk, A., Smirnov, A., Slutsker, I., Dickerson, R. R.,  
937 Thompson, A. M., and Schafer, J. S.: An analysis of AERONET aerosol absorption properties  
938 and classifications representative of aerosol source regions, *J. Geophys. Res. Atmos.*, 117, 1–  
939 16, <https://doi.org/10.1029/2012JD018127>, 2012.

940 Giles, D. M., Sinyuk, A., Sorokin, M. G., Schafer, J. S., Smirnov, A., Slutsker, I., Eck, T. F.,  
941 Holben, B. N., Lewis, J. R., Campbell, J. R., Welton, E. J., Korokin, S. V., and Lyapustin, A.  
942 I.: Advancements in the Aerosol Robotic Network (AERONET) Version 3 database –  
943 automated near-real-time quality control algorithm with improved cloud screening for Sun  
944 photometer aerosol optical depth (AOD) measurements, *Atmos. Meas. Tech.*, 12, 169–209,  
945 <https://doi.org/10.5194/amt-12-169-2019>, 2019.

946 Go, S., Kim, J., Park, S. S., Kim, M., Lim, H., Kim, J. Y., Lee, D. W., and Im, J.: Synergistic use  
947 of hyperspectral uv-visible omi and broadband meteorological imager modis data for a  
948 merged aerosol product, *Remote Sens.*, 12, 1–34, <https://doi.org/10.3390/rs12233987>, 2020.

949 Go, S., Lyapustin, A., Schuster, G. L., Choi, M., Ginoux, P., Chin, M., Kalashnikova, O., Dubovik,  
950 O., Kim, J., da Silva, A., Holben, B., and Reid, J. S.: Inferring iron-oxide species content in  
951 atmospheric mineral dust from DSCOVER EPIC observations, *Atmos. Chem. Phys.*, 22, 1395–  
952 1423, <https://doi.org/10.5194/acp-22-1395-2022>, 2022.

953 Gyawali, M., Arnott, W., Zaveri, R., Song, C., Flowers, B., Dubey, M., Setyan, A., Zhang, Q.,  
954 China, S., Mazzoleni, C., Gorkowski, K., Subramanian, R., and Moosmüller, H.: Evolution  
955 of Multispectral Aerosol Absorption Properties in a Biogenically-Influenced Urban  
956 Environment during the CARES Campaign, *Atmosphere (Basel)*, 8, 217,  
957 <https://doi.org/10.3390/atmos8110217>, 2017.

958 Haywood, J. M., Abel, S. J., Barrett, P. A., Bellouin, N., Blyth, A., Bower, K. N., Brooks, M.,  
959 Carslaw, K., Che, H., Coe, H., Cotterell, M. I., Crawford, I., Cui, Z., Davies, N., Dingley, B.,  
960 Field, P., Formenti, P., Gordon, H., de Graaf, M., Herbert, R., Johnson, B., Jones, A. C.,  
961 Langridge, J. M., Malavelle, F., Partridge, D. G., Peers, F., Redemann, J., Stier, P., Szpek, K.,  
962 Taylor, J. W., Watson-Parris, D., Wood, R., Wu, H., and Zuidema, P.: The CLOUD–Aerosol–  
963 Radiation Interaction and Forcing: Year 2017 (CLARIFY-2017) measurement campaign,  
964 *Atmos. Chem. Phys.*, 21, 1049–1084, <https://doi.org/10.5194/acp-21-1049-2021>, 2021.

965 Hess, M., Koepke, P., and Schult, I.: Optical Properties of Aerosols and Clouds: The Software  
966 Package OPAC, *Bull. Am. Meteorol. Soc.*, 79, 831–844, [https://doi.org/10.1175/1520-0477\(1998\)079<0831:OPOAAC>2.0.CO;2](https://doi.org/10.1175/1520-0477(1998)079<0831:OPOAAC>2.0.CO;2), 1998.

968 Hobbs, P. V., Reid, J. S., Kotchenruther, R. A., Ferek, R. J., and Weiss, R.: Direct Radiative  
969 Forcing by Smoke from Biomass Burning, *Science (80-. )*, 275, 1777–1778,  
970 <https://doi.org/10.1126/science.275.5307.1777>, 1997.

971 Hoffer, A., Gelencsér, A., Guyon, P., Kiss, G., Schmid, O., Frank, G. P., Artaxo, P., and Andreae,  
972 M. O.: Optical properties of humic-like substances (HULIS) in biomass-burning aerosols,  
973 *Atmos. Chem. Phys.*, 6, 3563–3570, <https://doi.org/10.5194/acp-6-3563-2006>, 2006.

974 Holben, B. N., Eck, T. F., Slutsker, I., Tanré, D., Buis, J. P., Setzer, A., Vermote, E., Reagan, J.  
975 A., Kaufman, Y. J., Nakajima, T., Lavenu, F., Jankowiak, I., and Smirnov, A.: AERONET—  
976 A Federated Instrument Network and Data Archive for Aerosol Characterization, *Remote  
977 Sens. Environ.*, 66, 1–16, [https://doi.org/10.1016/S0034-4257\(98\)00031-5](https://doi.org/10.1016/S0034-4257(98)00031-5), 1998.

978 IPCC: Climate Change 2021 – The Physical Science Basis, Cambridge University Press,  
979 <https://doi.org/10.1017/9781009157896>, 2023.

980 Jacobson, M. Z.: Strong radiative heating due to the mixing state of black carbon in atmospheric  
981 aerosols, *Nature*, 409, 695–697, <https://doi.org/10.1038/35055518>, 2001.

982 Jethva, H., Torres, O., and Ahn, C.: Global assessment of OMI aerosol single-scattering albedo  
983 using ground-based AERONET inversion, *J. Geophys. Res.*, 119, 9020–9040,  
984 <https://doi.org/10.1002/2014JD021672>, 2014.

985 Jo, D. S., Park, R. J., Lee, S., Kim, S. W., and Zhang, X.: A global simulation of brown carbon:  
986 Implications for photochemistry and direct radiative effect, *Atmos. Chem. Phys.*, 16, 3413–  
987 3432, <https://doi.org/10.5194/acp-16-3413-2016>, 2016.

988 Junghenn Noyes, K., Kahn, R., Sedlacek, A., Kleinman, L., Limbacher, J., and Li, Z.: Wildfire  
989 Smoke Particle Properties and Evolution, from Space-Based Multi-Angle Imaging, *Remote  
990 Sens.*, 12, 769, <https://doi.org/10.3390/rs12050769>, 2020a.

991 Junghenn Noyes, K. T., Kahn, R. A., Limbacher, J. A., Li, Z., Fenn, M. A., Giles, D. M., Hair, J.  
992 W., Katich, J. M., Moore, R. H., Robinson, C. E., Sanchez, K. J., Shingler, T. J., Thornhill,  
993 K. L., Wiggins, E. B., and Winstead, E. L.: Wildfire Smoke Particle Properties and Evolution,  
994 From Space-Based Multi-Angle Imaging II: The Williams Flats Fire during the FIREX-AQ  
995 Campaign, *Remote Sens.*, 12, 3823, <https://doi.org/10.3390/rs12223823>, 2020b.

996 Junghenn Noyes, K. T., Kahn, R. A., Limbacher, J. A., and Li, Z.: Canadian and Alaskan wildfire  
997 smoke particle properties, their evolution, and controlling factors, from satellite observations,  
998 *Atmos. Chem. Phys.*, 22, 10267–10290, <https://doi.org/10.5194/acp-22-10267-2022>, 2022.

999 Kahn, R. A., Berkoff, T. A., Brock, C., Chen, G., Ferrare, R. A., Ghan, S., Hansico, T. F., Hegg,  
1000 D. A., Martins, J. V., McNaughton, C. S., Murphy, D. M., Ogren, J. A., Penner, J. E.,  
1001 Pilewskie, P., Seinfeld, J. H., and Worsnop, D. R.: SAM-CAAM: A Concept for Acquiring  
1002 Systematic Aircraft Measurements to Characterize Aerosol Air Masses, *Bull. Am. Meteorol.*  
1003 *Soc.*, 98, 2215–2228, <https://doi.org/10.1175/BAMS-D-16-0003.1>, 2017.

1004 Kahn, R. A., Andrews, E., Brock, C. A., Chin, M., Feingold, G., Gettelman, A., Levy, R. C.,  
1005 Murphy, D. M., Nenes, A., Pierce, J. R., Popp, T., Redemann, J., Sayer, A. M., da Silva, A.  
1006 M., Sogacheva, L., and Stier, P.: Reducing Aerosol Forcing Uncertainty by Combining  
1007 Models With Satellite and Within-The-Atmosphere Observations: A Three-Way Street, *Rev.*  
1008 *Geophys.*, 61, <https://doi.org/10.1029/2022RG000796>, 2023.

1009 Kalashnikova, O. V., Garay, M. J., Bates, K. H., Kenseth, C. M., Kong, W., Cappa, C. D.,  
1010 Lyapustin, A. I., Jonsson, H. H., Seidel, F. C., Xu, F., Diner, D. J., and Seinfeld, J. H.:  
1011 Photopolarimetric Sensitivity to Black Carbon Content of Wildfire Smoke: Results From the  
1012 2016 ImPACT-PM Field Campaign, *J. Geophys. Res. Atmos.*, 123, 5376–5396,  
1013 <https://doi.org/10.1029/2017JD028032>, 2018.

1014 Kirchstetter, T. W., Novakov, T., and Hobbs, P. V.: Evidence that the spectral dependence of light  
1015 absorption by aerosols is affected by organic carbon, *J. Geophys. Res. D Atmos.*, 109, 1–12,  
1016 <https://doi.org/10.1029/2004JD004999>, 2004.

1017 Kleinman, L. I., Sedlacek III, A. J., Adachi, K., Buseck, P. R., Collier, S., Dubey, M. K., Hodshire,  
1018 A. L., Lewis, E., Onasch, T. B., Pierce, J. R., Shilling, J., Springston, S. R., Wang, J., Zhang,  
1019 Q., Zhou, S., and Yokelson, R. J.: Rapid evolution of aerosol particles and their optical  
1020 properties downwind of wildfires in the western US, *Atmos. Chem. Phys.*, 20, 13319–13341,  
1021 <https://doi.org/10.5194/acp-20-13319-2020>, 2020.

1022 Lack, D. A., Langridge, J. M., Bahreini, R., Cappa, C. D., Middlebrook, A. M., and Schwarz, J.  
1023 P.: Brown carbon and internal mixing in biomass burning particles, *Proc. Natl. Acad. Sci.*,  
1024 109, 14802–14807, <https://doi.org/10.1073/pnas.1206575109>, 2012.

1025 Laskin, A., Laskin, J., and Nizkorodov, S. A.: Chemistry of Atmospheric Brown Carbon, *Chem.*  
1026 *Rev.*, 115, 4335–4382, <https://doi.org/10.1021/cr5006167>, 2015.

1027 Lavoué, D., Liousse, C., Cachier, H., Stocks, B. J., and Goldammer, J. G.: Modeling of  
1028 carbonaceous particles emitted by boreal and temperate wildfires at northern latitudes, *J.*  
1029 *Geophys. Res. Atmos.*, 105, 26871–26890, <https://doi.org/10.1029/2000JD900180>, 2000.

1030 Lesins, G., Chylek, P., and Lohmann, U.: A study of internal and external mixing scenarios and  
1031 its effect on aerosol optical properties and direct radiative forcing, *J. Geophys. Res. Atmos.*,  
1032 107, <https://doi.org/10.1029/2001jd000973>, 2002.

1033 Levenberg, K.: A method for the solution of certain non-linear problems in least squares, *Q. Appl.*  
1034 *Math.*, 2, 164–168, <https://doi.org/10.1090/qam/10666>, 1944.

1035 Li, L., Dubovik, O., Derimian, Y., Schuster, G. L., Lapyonok, T., Litvinov, P., Ducos, F., Fuentès,  
1036 D., Chen, C., Li, Z., Lopatin, A., Torres, B., and Che, H.: Retrieval of aerosol components  
1037 directly from satellite and ground-based measurements, *Atmos. Chem. Phys.*, 19, 13409–  
1038 13443, <https://doi.org/10.5194/acp-19-13409-2019>, 2019.

1039 Li, L., Che, H., Derimian, Y., Dubovik, O., Schuster, G. L., Chen, C., Li, Q., Wang, Y., Guo, B.,  
1040 and Zhang, X.: Retrievals of fine mode light-absorbing carbonaceous aerosols from  
1041 POLDER/PARASOL observations over East and South Asia, *Remote Sens. Environ.*, 247,  
1042 111913, <https://doi.org/10.1016/j.rse.2020.111913>, 2020.

1043 Li, L., Derimian, Y., Chen, C., Zhang, X., Che, H., Schuster, G. L., Fuentès, D., Litvinov, P.,  
1044 Lapyonok, T., Lopatin, A., Matar, C., Ducos, F., Karol, Y., Torres, B., Gui, K., Zheng, Y.,

1045 Liang, Y., Lei, Y., Zhu, J., Zhang, L., Zhong, J., Zhang, X., and Dubovik, O.: Climatology of  
1046 aerosol component concentrations derived from multi-angular polarimetric POLDER-3  
1047 observations using GRASP algorithm, *Earth Syst. Sci. Data*, 14, 3439–3469,  
1048 <https://doi.org/10.5194/essd-14-3439-2022>, 2022.

1049 Liang, Y., Stamatis, C., Fortner, E. C., Wernis, R. A., Van Rooy, P., Majluf, F., Yacovitch, T. I.,  
1050 Daube, C., Herndon, S. C., Kreisberg, N. M., Barsanti, K. C., and Goldstein, A. H.: Emissions  
1051 of organic compounds from western US wildfires and their near-fire transformations, *Atmos.*  
1052 *Chem. Phys.*, 22, 9877–9893, <https://doi.org/10.5194/acp-22-9877-2022>, 2022.

1053 Lim, H.-J. and Turpin, B. J.: Origins of Primary and Secondary Organic Aerosol in Atlanta:  
1054 Results of Time-Resolved Measurements during the Atlanta Supersite Experiment, *Environ.*  
1055 *Sci. Technol.*, 36, 4489–4496, <https://doi.org/10.1021/es0206487>, 2002.

1056 Limbacher, J. A., Kahn, R. A., and Lee, J.: The new MISR research aerosol retrieval algorithm: a  
1057 multi-angle, multi-spectral, bounded-variable least squares retrieval of aerosol particle  
1058 properties over both land and water, *Atmos. Meas. Tech.*, 15, 6865–6887,  
1059 <https://doi.org/10.5194/amt-15-6865-2022>, 2022.

1060 Liu, D., He, C., Schwarz, J. P., and Wang, X.: Lifecycle of light-absorbing carbonaceous aerosols  
1061 in the atmosphere, *npj Clim. Atmos. Sci.*, 3, 40, [https://doi.org/10.1038/s41612-020-00145-](https://doi.org/10.1038/s41612-020-00145-8)  
1062 [8](https://doi.org/10.1038/s41612-020-00145-8), 2020.

1063 Liu, Y., Stanturf, J., and Goodrick, S.: Trends in global wildfire potential in a changing climate,  
1064 *For. Ecol. Manage.*, 259, 685–697, <https://doi.org/10.1016/j.foreco.2009.09.002>, 2010.

1065 Lyapustin, A., Wang, Y., Korkin, S., and Huang, D.: MODIS Collection 6 MAIAC algorithm,  
1066 *Atmos. Meas. Tech.*, 11, 5741–5765, <https://doi.org/10.5194/amt-11-5741-2018>, 2018.

1067 Lyapustin, A., Wang, Y., Go, S., Choi, M., Korkin, S., Huang, D., Knyazikhin, Y., Blank, K., and  
1068 Marshak, A.: Atmospheric Correction of DSCOVR EPIC: Version 2 MAIAC Algorithm,  
1069 *Front. Remote Sens.*, 2, 1–10, <https://doi.org/10.3389/frsen.2021.748362>, 2021a.

1070 Lyapustin, A., Go, S., Korkin, S., Wang, Y., Torres, O., Jethva, H., and Marshak, A.: Retrievals  
1071 of Aerosol Optical Depth and Spectral Absorption From DSCOVR EPIC, *Front. Remote*  
1072 *Sens.*, 2, 1–14, <https://doi.org/10.3389/frsen.2021.645794>, 2021b.

1073 Markel, V. A.: Introduction to the Maxwell Garnett approximation: tutorial, *J. Opt. Soc. Am. A*,  
1074 33, 1244, <https://doi.org/10.1364/josaa.33.001244>, 2016a.

1075 Markel, V. A.: Maxwell Garnett approximation (advanced topics): tutorial, *J. Opt. Soc. Am. A*, 33,  
1076 2237, <https://doi.org/10.1364/josaa.33.002237>, 2016b.

1077 Marquardt, D. W.: An Algorithm for Least-Squares Estimation of Nonlinear Parameters, *J. Soc.*  
1078 *Ind. Appl. Math.*, 11, 431–441, <https://doi.org/10.1137/0111030>, 1963.

1079 Marshak, A., Herman, J., Szabo, A., Blank, K., Carn, S., Cede, A., Geogdzhayev, I., Huang, D.,  
1080 Huang, L. K., Knyazikhin, Y., Kowalewski, M., Krotkov, N., Lyapustin, A., McPeters, R.,  
1081 Meyer, K. G., Torres, O., and Yang, Y.: Earth observations from DSCOVR epic instrument,  
1082 *Bull. Am. Meteorol. Soc.*, 99, 1829–1850, <https://doi.org/10.1175/BAMS-D-17-0223.1>, 2018.

1083 Mok, J., Krotkov, N. A., Arola, A., Torres, O., Jethva, H., Andrade, M., Labow, G., Eck, T. F., Li,  
1084 Z., Dickerson, R. R., Stenchikov, G. L., Osipov, S., and Ren, X.: Impacts of brown carbon  
1085 from biomass burning on surface UV and ozone photochemistry in the Amazon Basin, *Sci.*  
1086 *Rep.*, 6, 1–9, <https://doi.org/10.1038/srep36940>, 2016.

1087 Mok, J., Krotkov, N. A., Torres, O., Jethva, H., Li, Z., Kim, J., Koo, J. H., Go, S., Irie, H., Labow,  
1088 G., Eck, T. F., Holben, B. N., Herman, J., Loughman, R. P., Spinei, E., Soo Lee, S., Khatri,  
1089 P., and Campanelli, M.: Comparisons of spectral aerosol single scattering albedo in Seoul,  
1090 South Korea, *Atmos. Meas. Tech.*, 11, 2295–2311, <https://doi.org/10.5194/amt-11-2295->

1091 2018, 2018.

1092 Moosmüller, H., Chakrabarty, R. K., and Arnott, W. P.: Aerosol light absorption and its  
1093 measurement: A review, *J. Quant. Spectrosc. Radiat. Transf.*, 110, 844–878,  
1094 <https://doi.org/10.1016/j.jqsrt.2009.02.035>, 2009.

1095 Nanda, S., de Graaf, M., Veeffkind, J. P., Sneep, M., ter Linden, M., Sun, J., and Levelt, P. F.: A  
1096 first comparison of TROPOMI aerosol layer height (ALH) to CALIOP data, *Atmos. Meas.  
1097 Tech.*, 13, 3043–3059, <https://doi.org/10.5194/amt-13-3043-2020>, 2020.

1098 Pausas, J. G. and Keeley, J. E.: A Burning Story: The Role of Fire in the History of Life, *Bioscience*,  
1099 59, 593–601, <https://doi.org/10.1525/bio.2009.59.7.10>, 2009.

1100 Petters, M. D., Carrico, C. M., Kreidenweis, S. M., Prenni, A. J., DeMott, P. J., Collett, J. L., and  
1101 Moosmüller, H.: Cloud condensation nucleation activity of biomass burning aerosol, *J.  
1102 Geophys. Res. Atmos.*, 114, <https://doi.org/10.1029/2009JD012353>, 2009.

1103 Phillips, S. M. and Smith, G. D.: Light Absorption by Charge Transfer Complexes in Brown  
1104 Carbon Aerosols, *Environ. Sci. Technol. Lett.*, 1, 382–386, <https://doi.org/10.1021/ez500263j>,  
1105 2014.

1106 Pokhrel, R. P., Wagner, N. L., Langridge, J. M., Lack, D. A., Jayarathne, T., Stone, E. A.,  
1107 Stockwell, C. E., Yokelson, R. J., and Murphy, S. M.: Parameterization of single-scattering  
1108 albedo (SSA) and absorption Ångström exponent (AAE) with EC/OC for aerosol emissions  
1109 from biomass burning, *Atmos. Chem. Phys.*, 16, 9549–9561, <https://doi.org/10.5194/acp-16-9549-2016>, 2016.

1111 Press, W. H., Teukolsky, S. A., Vetterling, W. T., and Flannery, B. P.: Numerical Recipes 3rd  
1112 Edition: The Art of Scientific Computing, 3rd ed., Cambridge University Press, USA, 2007.

1113 Reid, J. S., Koppmann, R., Eck, T. F., and Eleuterio, D. P.: A review of biomass burning emissions  
1114 part II: intensive physical properties of biomass burning particles, *Atmos. Chem. Phys.*, 5,  
1115 799–825, <https://doi.org/10.5194/acp-5-799-2005>, 2005a.

1116 Reid, J. S., Eck, T. F., Christopher, S. A., Koppmann, R., Dubovik, O., Eleuterio, D. P., Holben,  
1117 B. N., Reid, E. A., and Zhang, J.: A review of biomass burning emissions part III: intensive  
1118 optical properties of biomass burning particles, *Atmos. Chem. Phys.*, 5, 827–849,  
1119 <https://doi.org/10.5194/acp-5-827-2005>, 2005b.

1120 Remer, L. A., Davis, A. B., Mattoo, S., Levy, R. C., Kalashnikova, O. V., Coddington, O.,  
1121 Chowdhary, J., Knobelspiesse, K., Xu, X., Ahmad, Z., Boss, E., Cairns, B., Dierssen, H. M.,  
1122 Diner, D. J., Franz, B., Frouin, R., Gao, B., Ibrahim, A., Martins, J. V., Omar, A. H., Torres,  
1123 O., Xu, F., and Zhai, P.-W.: Retrieving Aerosol Characteristics From the PACE Mission, Part  
1124 1: Ocean Color Instrument, *Front. Earth Sci.*, 7, 1–20,  
1125 <https://doi.org/10.3389/feart.2019.00152>, 2019a.

1126 Remer, L. A., Knobelspiesse, K., Zhai, P., Xu, F., Kalashnikova, O. V., Chowdhary, J., Hasekamp,  
1127 O., Dubovik, O., Wu, L., Ahmad, Z., Boss, E., Cairns, B., Coddington, O., Davis, A. B.,  
1128 Dierssen, H. M., Diner, D. J., Franz, B., Frouin, R., Gao, B., Ibrahim, A., Levy, R. C., Martins,  
1129 J. V., Omar, A. H., and Torres, O.: Retrieving Aerosol Characteristics From the PACE  
1130 Mission, Part 2: Multi-Angle and Polarimetry, *Front. Environ. Sci.*, 7, 1–21,  
1131 <https://doi.org/10.3389/fenvs.2019.00094>, 2019b.

1132 Rios, B., Díaz-Esteban, Y., and Raga, G. B.: Smoke emissions from biomass burning in Central  
1133 Mexico and their impact on air quality in Mexico City: May 2019 case study, *Sci. Total  
1134 Environ.*, 904, 166912, <https://doi.org/10.1016/j.scitotenv.2023.166912>, 2023.

1135 Rissler, J., Vestin, A., Swietlicki, E., Fisch, G., Zhou, J., Artaxo, P., and Andreae, M. O.: Size  
1136 distribution and hygroscopic properties of aerosol particles from dry-season biomass burning

1137 in Amazonia, *Atmos. Chem. Phys.*, 6, 471–491, <https://doi.org/10.5194/acp-6-471-2006>,  
1138 2006.

1139 Samset, B. H., Stjern, C. W., Andrews, E., Kahn, R. A., Myhre, G., Schulz, M., and Schuster, G.  
1140 L.: Aerosol Absorption: Progress Towards Global and Regional Constraints, *Curr. Clim.*  
1141 *Chang. Reports*, 4, 65–83, <https://doi.org/10.1007/s40641-018-0091-4>, 2018.

1142 Sayer, A. M., Hsu, N. C., Eck, T. F., Smirnov, A., and Holben, B. N.: AERONET-based models  
1143 of smoke-dominated aerosol near source regions and transported over oceans, and  
1144 implications for satellite retrievals of aerosol optical depth, *Atmos. Chem. Phys.*, 14, 11493–  
1145 11523, <https://doi.org/10.5194/acp-14-11493-2014>, 2014.

1146 Sayer, A. M., Hsu, N. C., Lee, J., Kim, W. V., Burton, S., Fenn, M. A., Ferrare, R. A.,  
1147 Kacenelenbogen, M., LeBlanc, S., Pistone, K., Redemann, J., Segal-Rozenhaimer, M.,  
1148 Shinozuka, Y., and Tsay, S.: Two decades observing smoke above clouds in the south-eastern  
1149 Atlantic Ocean: Deep Blue algorithm updates and validation with ORACLES field campaign  
1150 data, *Atmos. Meas. Tech.*, 12, 3595–3627, <https://doi.org/10.5194/amt-12-3595-2019>, 2019.

1151 Schroeder, W. and Giglio, L.: VIIRS/NPP Thermal Anomalies/Fire Daily L3 Global 1km SIN  
1152 Grid V001. distributed by NASA EOSDIS Land Processes DAAC,  
1153 [doi:10.5067/VIIRS/VNP14A1.001](https://doi.org/10.5067/VIIRS/VNP14A1.001), 2018.

1154 Schuster, G. L., Dubovik, O., Holben, B. N., and Clothiaux, E. E.: Inferring black carbon content  
1155 and specific absorption from Aerosol Robotic Network (AERONET) aerosol retrievals, *J.*  
1156 *Geophys. Res. D Atmos.*, 110, 1–19, <https://doi.org/10.1029/2004JD004548>, 2005.

1157 Schuster, G. L., Dubovik, O., and Arola, A.: Remote sensing of soot carbon – Part 1:  
1158 Distinguishing different absorbing aerosol species, *Atmos. Chem. Phys.*, 16, 1565–1585,  
1159 <https://doi.org/10.5194/acp-16-1565-2016>, 2016.

1160 Schwarz, J. P., Gao, R. S., Spackman, J. R., Watts, L. A., Thomson, D. S., Fahey, D. W., Ryerson,  
1161 T. B., Peischl, J., Holloway, J. S., Trainer, M., Frost, G. J., Baynard, T., Lack, D. A., de Gouw,  
1162 J. A., Warneke, C., and Del Negro, L. A.: Measurement of the mixing state, mass, and optical  
1163 size of individual black carbon particles in urban and biomass burning emissions, *Geophys.*  
1164 *Res. Lett.*, 35, <https://doi.org/10.1029/2008GL033968>, 2008.

1165 Seiler, W. and Crutzen, P. J.: Estimates of gross and net fluxes of carbon between the biosphere  
1166 and the atmosphere from biomass burning, *Clim. Change*, 2, 207–247,  
1167 <https://doi.org/10.1007/BF00137988>, 1980.

1168 Sengupta, D., Samburova, V., Bhattarai, C., Kirillova, E., Mazzoleni, L., Iaukea-Lum, M., Watts,  
1169 A., Moosmüller, H., and Khlystov, A.: Light absorption by polar and non-polar aerosol  
1170 compounds from laboratory biomass combustion, *Atmos. Chem. Phys.*, 18, 10849–10867,  
1171 <https://doi.org/10.5194/acp-18-10849-2018>, 2018.

1172 Sengupta, D., Samburova, V., Bhattarai, C., Watts, A. C., Moosmüller, H., and Khlystov, A. Y.:  
1173 Polar semivolatile organic compounds in biomass-burning emissions and their chemical  
1174 transformations during aging in an oxidation flow reactor, *Atmos. Chem. Phys.*, 20, 8227–  
1175 8250, <https://doi.org/10.5194/acp-20-8227-2020>, 2020.

1176 Sinyuk, A., Holben, B. N., Eck, T. F., Giles, D. M., Slutsker, I., Korkin, S., Schafer, J. S., Smirnov,  
1177 A., Sorokin, M., and Lyapustin, A.: The AERONET Version 3 aerosol retrieval algorithm,  
1178 associated uncertainties and comparisons to Version 2, *Atmos. Meas. Tech.*, 13, 3375–3411,  
1179 <https://doi.org/10.5194/amt-13-3375-2020>, 2020.

1180 Sinyuk, A., Holben, B. N., Eck, T. F., Giles, D. M., Slutsker, I., Dubovik, O., Schafer, J. S.,  
1181 Smirnov, A., and Sorokin, M.: Employing relaxed smoothness constraints on imaginary part  
1182 of refractive index in AERONET aerosol retrieval algorithm, *Atmos. Meas. Tech.*, 15, 4135–

1183 4151, <https://doi.org/10.5194/amt-15-4135-2022>, 2022.

1184 Sumlin, B. J., Heinson, Y. W., Shetty, N., Pandey, A., Pattison, R. S., Baker, S., Hao, W. M., and  
1185 Chakrabarty, R. K.: UV–Vis–IR spectral complex refractive indices and optical properties of  
1186 brown carbon aerosol from biomass burning, *J. Quant. Spectrosc. Radiat. Transf.*, 206, 392–  
1187 398, <https://doi.org/10.1016/j.jqsrt.2017.12.009>, 2018.

1188 Sun, H., Biedermann, L., and Bond, T. C.: Color of brown carbon: A model for ultraviolet and  
1189 visible light absorption by organic carbon aerosol, *Geophys. Res. Lett.*, 34, L17813,  
1190 <https://doi.org/10.1029/2007GL029797>, 2007.

1191 Swap, R. J., Annegarn, H. J., Suttles, J. T., King, M. D., Platnick, S., Privette, J. L., and Scholes,  
1192 R. J.: Africa burning: A thematic analysis of the Southern African Regional Science Initiative  
1193 (SAFARI 2000), *J. Geophys. Res. Atmos.*, 108, n/a-n/a,  
1194 <https://doi.org/10.1029/2003JD003747>, 2003.

1195 Torres, O., Bhartia, P. K., Herman, J. R., Ahmad, Z., and Gleason, J.: Derivation of aerosol  
1196 properties from satellite measurements of backscattered ultraviolet radiation: Theoretical  
1197 basis, *J. Geophys. Res. Atmos.*, 103, 17099–17110, <https://doi.org/10.1029/98JD00900>, 1998.

1198 Torres, O., Tanskanen, A., Veihelmann, B., Ahn, C., Braak, R., Bhartia, P. K., Veeffkind, P., and  
1199 Levelt, P.: Aerosols and surface UV products from Ozone Monitoring Instrument  
1200 observations: An overview, *J. Geophys. Res. Atmos.*, 112, 1–14,  
1201 <https://doi.org/10.1029/2007JD008809>, 2007.

1202 Torres, O., Ahn, C., and Chen, Z.: Improvements to the OMI near-UV aerosol algorithm using A-  
1203 train CALIOP and AIRS observations, *Atmos. Meas. Tech.*, 6, 3257–3270,  
1204 <https://doi.org/10.5194/amt-6-3257-2013>, 2013.

1205 Torres, O., Jethva, H., Ahn, C., Jaross, G., and Loyola, D. G.: TROPOMI aerosol products:  
1206 Evaluation and observations of synoptic-scale carbonaceous aerosol plumes during 2018-  
1207 2020, *Atmos. Meas. Tech.*, 13, 6789–6806, <https://doi.org/10.5194/amt-13-6789-2020>, 2020.

1208 Tritscher, T., Jurányi, Z., Martin, M., Chirico, R., Gysel, M., Heringa, M. F., DeCarlo, P. F., Sierau,  
1209 B., Prévôt, A. S. H., Weingartner, E., and Baltensperger, U.: Changes of hygroscopicity and  
1210 morphology during ageing of diesel soot, *Environ. Res. Lett.*, 6, 034026,  
1211 <https://doi.org/10.1088/1748-9326/6/3/034026>, 2011.

1212 Turpin, B. J. and Lim, H.-J.: Species Contributions to PM<sub>2.5</sub> Mass Concentrations: Revisiting  
1213 Common Assumptions for Estimating Organic Mass, *Aerosol Sci. Technol.*, 35, 602–610,  
1214 <https://doi.org/10.1080/02786820119445>, 2001.

1215 Wang, L., Li, Z., Tian, Q., Ma, Y., Zhang, F., Zhang, Y., Li, D., Li, K., and Li, L.: Estimate of  
1216 aerosol absorbing components of black carbon, brown carbon, and dust from ground-based  
1217 remote sensing data of sun-sky radiometers, *J. Geophys. Res. Atmos.*, 118, 6534–6543,  
1218 <https://doi.org/10.1002/jgrd.50356>, 2013.

1219 Wang, X., Heald, C. L., Sedlacek, A. J., de Sá, S. S., Martin, S. T., Alexander, M. L., Watson, T.  
1220 B., Aiken, A. C., Springston, S. R., and Artaxo, P.: Deriving brown carbon from  
1221 multiwavelength absorption measurements: method and application to AERONET and  
1222 Aethalometer observations, *Atmos. Chem. Phys.*, 16, 12733–12752,  
1223 <https://doi.org/10.5194/acp-16-12733-2016>, 2016.

1224 Ward, D. E., Hao, W. M., Susott, R. A., Babbitt, R. E., Shea, R. W., Kauffman, J. B., and Justice,  
1225 C. O.: Effect of fuel composition on combustion efficiency and emission factors for African  
1226 savanna ecosystems, *J. Geophys. Res. Atmos.*, 101, 23569–23576,  
1227 <https://doi.org/10.1029/95JD02595>, 1996.

1228 van der Werf, G. R., Randerson, J. T., Giglio, L., Collatz, G. J., Mu, M., Kasibhatla, P. S., Morton,



1229 D. C., DeFries, R. S., Jin, Y., and van Leeuwen, T. T.: Global fire emissions and the  
1230 contribution of deforestation, savanna, forest, agricultural, and peat fires (1997–2009), *Atmos.*  
1231 *Chem. Phys.*, 10, 11707–11735, <https://doi.org/10.5194/acp-10-11707-2010>, 2010.

1232 van der Werf, G. R., Randerson, J. T., Giglio, L., van Leeuwen, T. T., Chen, Y., Rogers, B. M.,  
1233 Mu, M., van Marle, M. J. E., Morton, D. C., Collatz, G. J., Yokelson, R. J., and Kasibhatla,  
1234 P. S.: Global fire emissions estimates during 1997–2016, *Earth Syst. Sci. Data*, 9, 697–720,  
1235 <https://doi.org/10.5194/essd-9-697-2017>, 2017.

1236 Wooster, M. J., Roberts, G. J., Giglio, L., Roy, D., Freeborn, P., Boschetti, L., Justice, C., Ichoku,  
1237 C., Schroeder, W., Davies, D., Smith, A., Setzer, A., Csiszar, I., Strydom, T., Frost, P., Zhang,  
1238 T., Xu, W., de Jong, M., Johnston, J., Ellison, L., Vadrevu, K., McCarty, J., Tanpipat, V.,  
1239 Schmidt, C., and San-Miguel, J.: Satellite remote sensing of active fires: History and current  
1240 status, applications and future requirements, <https://doi.org/10.1016/j.rse.2021.112694>, 15  
1241 December 2021.

1242 Xiong, R., Li, J., Zhang, Y., Zhang, L., Jiang, K., Zheng, H., Kong, S., Shen, H., Cheng, H., Shen,  
1243 G., and Tao, S.: Global brown carbon emissions from combustion sources, *Environ. Sci.*  
1244 *Ecotechnology*, 12, 100201, <https://doi.org/10.1016/j.ese.2022.100201>, 2022.

1245 Xu, X., Wang, J., Wang, Y., Zeng, J., Torres, O., Reid, J. S., Miller, S. D., Martins, J. V., and  
1246 Remer, L. A.: Detecting layer height of smoke aerosols over vegetated land and water  
1247 surfaces via oxygen absorption bands: hourly results from EPIC/DSCOVR in deep space,  
1248 *Atmos. Meas. Tech.*, 12, 3269–3288, <https://doi.org/10.5194/amt-12-3269-2019>, 2019.

1249 Yu, H., Liu, S. C., and Dickinson, R. E.: Radiative effects of aerosols on the evolution of the  
1250 atmospheric boundary layer, *J. Geophys. Res. Atmos.*, 107,  
1251 <https://doi.org/10.1029/2001JD000754>, 2002.

1252 Zhang, A., Wang, Y., Zhang, Y., Weber, R. J., Song, Y., Ke, Z., and Zou, Y.: Modeling the global  
1253 radiative effect of brown carbon: a potentially larger heating source in the tropical free  
1254 troposphere than black carbon, *Atmos. Chem. Phys.*, 20, 1901–1920,  
1255 <https://doi.org/10.5194/acp-20-1901-2020>, 2020.

1256